

WL-TR-97-2079

PARTICLE IMAGE VELOCIMETRY



S. DASGUPTA  
T.H. CHEN  
W. TERRY

TAITECH, INCORPORATED  
3675 HARMELING DRIVE  
BEAVERCREEK, OH 45440-3568

JANUARY 1997

FINAL REPORT FOR 07/07/94-12/31/96

**THIS IS A SMALL BUSINESS INNOVATION RESEARCH (SBIR) PHASE II REPORT**

APPROVED FOR PUBLIC RELEASE; DISTRIBUTION IS UNLIMITED.

19971230 012

AEROPROPULSION AND POWER DIRECTORATE  
WRIGHT LABORATORY  
AIR FORCE MATERIEL COMMAND  
WRIGHT PATTERSON AFB OH 45433-7251

DTIC QUALITY INSPECTED 4

## NOTICE


USING GOVERNMENT DRAWINGS, SPECIFICATIONS, OR OTHER DATA INCLUDED IN THIS DOCUMENT FOR ANY PURPOSE OTHER THAN GOVERNMENT PROCUREMENT DOES NOT IN ANY WAY OBLIGATE THE US GOVERNMENT. THE FACT THAT THE GOVERNMENT FORMULATED OR SUPPLIED THE DRAWINGS, SPECIFICATIONS, OR OTHER DATA DOES NOT LICENSE THE HOLDER OR ANY OTHER PERSON OR CORPORATION; OR CONVEY ANY RIGHTS OR PERMISSION TO MANUFACTURE, USE, OR SELL ANY PATENTED INVENTION THAT MAY RELATE TO THEM.

THIS REPORT IS RELEASABLE TO THE NATIONAL TECHNICAL INFORMATION SERVICE (NTIS). AT NTIS, IT WILL BE AVAILABLE TO THE GENERAL PUBLIC, INCLUDING FOREIGN NATIONS.

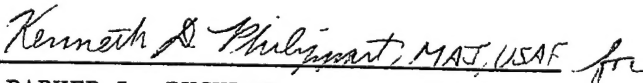
THIS TECHNICAL REPORT HAS BEEN REVIEWED AND IS APPROVED FOR PUBLICATION.



ABDOLLAH S. NEJAD  
Contract Monitor  
Experimental Research Branch  
Advanced Propulsion Division



ABDOLLAH S. NEJAD  
Chief  
Experimental Research Branch  
Advanced Propulsion Division



PARKER L. BUCKLEY  
Acting Chief  
Advanced Propulsion Division

IF YOUR ADDRESS HAS CHANGED, IF YOU WISH TO BE REMOVED FROM OUR MAILING LIST, OR IF THE ADDRESSEE IS NO LONGER EMPLOYED BY YOUR ORGANIZATION PLEASE NOTIFY WL/ POPT WRIGHT-PATTERSON AFB OH 45433-7251 TO HELP MAINTAIN A CURRENT MAILING LIST.

Do not return copies of this report unless contractual obligations or notice on a specific document requires its return.

REPORT DOCUMENTATION PAGE			Form Approved OMB No. 0704-0188	
Public reporting burden for this collection of information is estimated to average 1 hour per response, including the time for reviewing instructions, searching existing data sources, gathering and maintaining the data needed, and completing and reviewing the collection of information. Send comments regarding this burden estimate or any other aspect of this collection of information, including suggestions for reducing this burden, to Washington Headquarters Services, Directorate for Information Operations and Reports, 1215 Jefferson Davis Highway, Suite 1204, Arlington, VA 22202-4302, and to the Office of Management and Budget, Paperwork Reduction Project (0704-0188), Washington, DC 20503.				
1. AGENCY USE ONLY (Leave blank)		2. REPORT DATE 17 January 1997		3. REPORT TYPE AND DATES COVERED Final Report (7 Jul 94 - 31 Dec 96)
4. TITLE AND SUBTITLE  Particle Imaging Velocimetry			5. FUNDING NUMBERS C: F33615-94-C-2470 PE: 65502F PR: 3005 TA: 02 WU: JL	
6. AUTHOR(S)  S. Dasgupta, T. H. Chen, and W. Terry				
7. PERFORMING ORGANIZATION NAME(S) AND ADDRESS(ES)  Taitech, Incorporated 3675 Harmeling Drive Beavercreek OH 45440-3568			8. PERFORMING ORGANIZATION REPORT NUMBER  TI97RF-700	
9. SPONSORING/MONITORING AGENCY NAME(S) AND ADDRESS(ES) Aero Propulsion and Power Directorate Wright Laboratory Air Force Material Command Wright-Patterson AFB OH 45433-7251 POC: Diana D. Glawe WL/POPT, 937-255-9991			10. SPONSORING/MONITORING AGENCY REPORT NUMBER  WL-TR-97-2079	
11. SUPPLEMENTARY NOTES				
12a. DISTRIBUTION AVAILABILITY STATEMENT  Approved for public release; distribution is unlimited.			12b. DISTRIBUTION CODE	
13. ABSTRACT (Maximum 200 words)  Report developed under SBIR contract.  A two-color particle imaging velocimetry system was demonstrated for obtaining two-dimensional velocity measurements in a subsonic reacting flow and in a supersonic flowfield. Data was obtained using three different camera systems, an 8-mm video camera, a digital color CCD camera system and a 35-mm camera. The data obtained from the wall boundary layer region in the supersonic wind tunnel showed good correlation with LDV data. The flow in the wake region of the flameholder was investigated using the PIV system developed. The results obtained through these experiments showed that the PIV system was capable of resolving the flow information in the highly turbulent region with a high degree of accuracy. Values of shear layer stresses behind the bluff body region were also calculated from the PIV data. Reacting flow experiments showed the ability of the PIV system to resolve velocity fields in a highly turbulent, large gradient flow regime. The software yielded RMS fluctuations in the 1.5% range which is less than the 3% limit widely reported in the literature. Taitech, Inc. is currently commercializing the PIV system developed in this contract.				
14. SUBJECT TERMS combustor, laser diagnostics, PIV, LDV, velocimetry measurement, combustion  SBIR REPORT			15. NUMBER OF PAGES 73	
			16. PRICE CODE	
17. SECURITY CLASSIFICATION OF REPORT  UNCLASSIFIED	18. SECURITY CLASSIFICATION OF THIS PAGE  UNCLASSIFIED	19. SECURITY CLASSIFICATION OF ABSTRACT  UNCLASSIFIED	20. LIMITATION OF ABSTRACT  SAR	

<b>1. INTRODUCTION</b>	<b>4</b>
<b>2. MOTIVATION</b>	<b>4</b>
<b>3. PARTICLE IMAGING VELOCIMETRY FUNDAMENTALS</b>	<b>7</b>
3.1 LIGHT SCATTERING FROM PARTICLES	10
3.2 RESOLUTION OF PARTICLE MOTION	12
<b>4. INSTRUMENTATION DEVELOPMENT</b>	<b>12</b>
4.1 OVERALL PIV SYSTEM	13
4.1.1 LASERS	13
4.1.2 RAMAN CELL	15
4.1.3 OPTICS	15
4.2 TIME DELAY ADJUSTMENT	19
4.3 IMAGE ACQUISITION SYSTEMS	22
4.4 CAMERA INTERFACE	23
<b>5. ANALYSIS SOFTWARE</b>	<b>24</b>
5.1 THEORY OF DIGITAL PIV (DPIV)	24
5.2 ANALYSIS PROCEDURE	28
5.3 SOFTWARE TESTING	32
<b>6. PIV SYSTEM VALIDATION</b>	<b>35</b>
6.1 SUPERSONIC EXPERIMENTS	36
6.1.1 WIND TUNNEL TEST FACILITY	36
6.1.2 FLOW SEEDING	37
6.1.3 DATA ACQUISITION AND ANALYSIS FOR SUPERSONIC EXPERIMENTS	38
<b>7. STATISTICAL CALCULATIONS USING PIV MEASUREMENTS</b>	<b>42</b>
7.1 DATA ANALYSIS	42
7.2 UNCERTAINTY ANALYSIS	43
7.2.1 RESULTS OF UNCERTAINTY ANALYSIS	43
<b>8. FLOW BEHIND A BLUFF BODY COMBUSTOR</b>	<b>54</b>



8.1 DATA ACQUISITION	55
8.2 NON-REACTING FLOW BEHIND A BLUFF BODY - PIV DATA ANALYSIS	58
8.3 STATISTICAL CALCULATIONS OF FLOW PARAMETERS	61
8.4 BOUNDARY LAYER EXPERIMENTS	65
9. REACTING FLOW EXPERIMENTS	65
10. CONCLUSIONS	67
11. REFERENCES	68
12. APPENDICES	71

## PARTICLE IMAGING VELOCIMETRY

### Final Report

This report covers work performed during the period 1 September 1994 to 31 August 1996, under Air Force Contract F33615-94-C-2470, entitled "Particle Imaging Velocimetry." Taitech personnel contributing to this effort were Tzong H. Chen, Samhita Dasgupta, William Terry and William E. Eakins. The work described was completed at the Aero Propulsion and Power Directorate of Wright Laboratory (WL/PO), at Wright Patterson Air Force Base.

## **1. INTRODUCTION**

This Phase II program has developed a prototype two-color Particle Imaging Velocimetry System for use in supersonic and combustng flowfields. This system permits the instantaneous 2D measurement of particle velocities in a supersonic and/or reacting flow field. The Phase II objectives were developed based on the results obtained in the Phase I portion of this program, including the development of specialized image processing software for obtaining 2-dimensional velocity maps from the collected data and the development of a portable, turn-key two-color PIV system that can be used in a wide range of combustng flowfields. The initial development of the PIV system hardware was completed in the fourth quarter of the Phase II program. Since the fifth quarter of the Phase II program, experiments have been carried out in a series of different flowfields in order to characterize the beam delivery mechanism, the imaging and the image processing software. A brief motivation for this work is presented below, followed by a description of the work performed and a discussion of the results obtained.

## **2. MOTIVATION**

In studies of hydrocarbon scramjet propulsion systems, one of the typical flow conditions encountered is a dense fuel spray in a high-speed crossflow. The flowfield is turbulent and two-phase in nature and is often associated with transition phenomena (e.g., the fuel may be preheated and pressurized to become supercritical). The flowfield becomes even more complicated when combustion is involved. To understand the complex mixing and combustion phenomena in the multi-phase environment, an instantaneous two-dimensional (2-D) survey of the fluid properties (i.e., temperature, gas velocity, fuel droplet size and velocity, number density, species concentration, and pressure) is usually preferred over conventional point measurements. Some of the more recent developments and applications of laser diagnostics for measuring the above properties in supersonic flows are summarized below.

For 2-D velocity measurements, Klavuhn et al. [1992] implemented an OH laser-induced fluorescence (LIF) technique in high-speed reacting flows. The velocity component in the plane of the laser sheet was determined from the Doppler shift of the OH LIF. Allen et al. [1992] implemented a similar approach in a study of a supersonic reacting flow. An alternate approach is the so-called filtered Rayleigh scattering technique; this is a potentially powerful technique for 2-D velocity measurements [Miles et al. 1992, Elliott et al. 1993, Shirley and Winter 1993], but its efficacy has not been proved. For species concentration measurements, Nandula et al. [1992] used a KrF excimer laser to study the multi-species transport of an H<sub>2</sub>-air flame; Quagliaroli et al. [1992] employed a KrF excimer laser for 2-D imaging of OH LIF in a supersonic combustion tunnel; Messersmith and Dutton [1992] applied LIF to measure scalar transport in compressible mixing layers; Yip et al. [1993] used acetone and biacetyl LIF for 2-D concentration measurements in jet flows; Allen et al. [1993], McMillin et al. [1992, 1993], Grinstead et al. [1993], and Seitzman et al. [1993] used NO and O<sub>2</sub> LIF for 2-D temperature measurements; and finally, Miles et al. [1993] performed 1-D temperature measurements using the LIF technique.

For the past five years, several laser diagnostic techniques for 2-D measurements have been developed and implemented at WL/POPT. These techniques include (1) particle imaging velocimetry (PIV) for measuring particle velocity [Goss et al. 1991, Chen et al. 1993, Driscoll et al. 1993]; (2) OH-Flow-Tagging Velocimetry (OFTV) for measuring gas velocity [Goss et al. 1991, Chen et al. 1991]; (3) LIF for measuring OH, CN, and CH concentrations [Chen and Goss 1991, Goss et al. 1992]; and (4) Rayleigh scattering for measuring density. The groundwork for measuring temperature two-dimensionally using two-line OH fluorescence was also accomplished.

Two-dimensional measurement techniques are not necessarily more complicated than point measurement techniques, though there may be a trade-off between accuracy and 2-D measurement capability. The 2-D techniques may be better suited to the harsh environments of high-speed combustion facilities since PIV techniques can be used in particulate laden environments whereas LDV is not suited for such

flowfields. Fortunately, the above diagnostics share common hardware components, such as an Nd:YAG, dye and excimer lasers, intensified CCD camera, camera controller, synchronization electronics, and UV optics. The data analysis procedures also have many steps in common. With these elements now established at the Aero Propulsion and Power Directorate, it is desirable to combine and extend these techniques towards a better understanding of fuel injection, atomization, mixing, and combustion.

One of the difficult issues in the study of supersonic fuel injection is the droplet-turbulence interaction. Recently, Chen et al. [1993a] confirmed that the phase change in the initial spray region can be a dominant factor in determining fuel penetration. The spatial variation of the slip velocity among liquid fragments, droplets, and the gas stream can be dramatic. In addition, a recent experiment performed by Taitech, Inc. has demonstrated that a phase change can occur in the fuel passage prior to injection and that this phenomenon can be intermittent, leading to different modes of jet behavior. For the same liquid exit velocity, the initial jet region of the spray plume can be in the form of a liquid column, which penetrates deep into the freestream. It was found, on the other hand, that the initial liquid core can sometimes contain cavitation bubbles, and that the resulting jet showed better atomization characteristics (see also Sher and Elata 1977, Marek and Cooper 1980, Solomon et al. 1985, and Lefebvre et al. 1994). Therefore, the major thrust for the Phase I study of this project was to investigate the feasibility of combining 2-D measurement schemes suitable for simultaneous measurement of multi-phase properties. In Phase I of this SBIR project, the feasibility of combining two 2D measurement schemes was demonstrated through the combined PIV and OH flow tagging experiment. In Phase II, the effort was concentrated on making the PIV system commercializable, i.e. the system was made portable and user friendly.

Obtaining instantaneous velocity information in a complex flowfield is a difficult task. One of the methods that has gained popularity in the past 5 - 10 years is Particle Imaging Velocimetry (PIV). One of the main advantages of PIV is that it

is a two-dimensional instantaneous technique unlike LDV which is a point measurement technique. Thus, 2D and even 3D velocity maps can be obtained in a fraction of the time it takes to perform a complete velocity map using LDV. The feasibility of using the PIV technique to study flow phenomena has been widely demonstrated, although the capability to perform these measurements in complex flowfields such as supersonic and combustor flowfields have not been consistently demonstrated. A turn-key PIV system is extremely useful for wind tunnel test measurements for reacting and non-reacting flowfields.

### 3. PARTICLE IMAGING VELOCIMETRY FUNDAMENTALS

Typical PIV data are obtained by recording double images of particles within a flow through illumination with a pulsed laser sheet. A thin slice of the flowfield is illuminated by a pulsed laser. Assuming that the x and y coordinates of the flowfield coordinate system extend along the long dimensions of the laser sheet with the center situated within the thickness of the laser sheet. The laser sheet is placed parallel to the main flow direction so that the probability of obtaining two images of the same particle within a snapshot are enhanced. The in-plane displacement of the particle in the flowfield is given by

$$X = \Delta x \hat{x} + \Delta y \hat{y} \quad (3.1)$$

where  $\Delta x$  and  $\Delta y$  are the magnitudes of the particle displacements in the x- and y-directions, respectively. A planar image field is then formed at the camera image plane by a lens with linear magnification  $m$ . The camera image is captured on either photographic film or a video camera detector array, completing the acquisition process.

Following image acquisition, the flow velocities can then be determined from the recorded particle displacement in the camera image plane.  $X \cdot m$ , and knowing the camera magnification  $m$  or the image resolution, the displacement may be

determined. Given the pulse time separation  $\Delta t$ , the flow velocity vector at that point is

$$U = \frac{X}{\Delta t} \quad (3.2)$$

where

$$U = u\hat{x} + v\hat{y} \quad (3.3)$$

and  $u$  and  $v$  are the in plane velocity coordinates.

The velocities at each of the locations in the flowfield are found by breaking the image area up into small regions known as *interrogation spots*. The mean particle displacement within an individual spot determines the velocity vector at that particular location. The interrogation spot defines the effective probe volume in the test region when the interrogation spot is mapped back into the actual flowfield. In this instance, the probe volume for the PIV data is  $s^2t$  where  $s$  is the  $x$  and  $y$  edge dimension measured in the flowfield and  $t$  is the laser sheet thickness. The resolution of the PIV data is determined by the probe volume.

The particle image size is also a limiting factor for the capabilities of a PIV system. The particle image size defines the smallest measureable displacement is limited to the diameter of the seed particle so that there is no overlap. The maximum measureable displacement is also limited by the finite size of the interrogation spot. The maximum displacement is typically 25% to 30% of the interrogation spot dimension (Keane and Adrian 1990). The dynamic range of the system is defined by the maximum and minimum displacement. In high speed and complex flowfields, large velocity gradients are common, high spatial resolution is required which limits the size of the interrogation spot.

In a typical PIV system, the projection of the particle image diameter projected in the flowfield plane ( $d_i$ ) is not equal to the original particle diameter ( $d_p$ ). The effective diameter of a focussed particle image can be approximated by (Adrian 1991)

$$d_e = \left( d_p^2 + \frac{d_s^2}{m^2} \right)^{1/2} \quad (3.4)$$

where  $m$  is the linear magnification of the camera and  $d_s$  the diffraction limited spot diameter of the camera lens. For all the PIV applications described in this report, the particle diameters were less than  $5 \mu\text{m}$ , for which the only significant term in the above equation is  $d_s$ . This term may be obtained by determining the Airy function profile for the given lens. In the camera image plane,  $d_s$  is given by (Adrian 1991)

$$d_s = 2.44(1+m)f^{\#}\lambda \quad (3.5)$$

or in flowfield coordinates.

$$d_{s,f} = 2.44 \left( \frac{1}{m} + 1 \right) f^{\#}\lambda \quad (3.6)$$

where  $f^{\#}$  is the lens aperture number and  $\lambda$  is the wavelength of the light source. In the experiments described in this report, the wavelength for both the pulses have to be considered, a mean value between the two wavelengths was chosen.

The next effect that determines the image diameter is the response of the imaging medium (film, digital camera or video camera) to the wavelength of the PIV beams. Assuming the seed particles are spherical, and the PIV images are collected at right angles to the scattering illumination, and the particle size is the same order as the laser wavelength  $\lambda$ , the mean exposure of the particle image  $\bar{\epsilon}$  is approximated from Mie scattering theory as (Adrian and Yao 1985)

$$\bar{\epsilon} = \frac{Ed_p^3 D_a^4}{wt S_0^2 S_i^2 \lambda^3} \quad (3.7)$$



where  $E$  is the pulse energy of the illuminating laser, and  $D_a$  is the aperture diameter of the camera lens. Since the collected images are all focussed images, the effects due to the depth of field of the camera have to be examined also. The depth of field for a camera lens is given by (Adrian 1991)

$$\delta z = 4 \left( 1 + \frac{1}{m} \right)^2 f^{\#2} \lambda \quad (3.8)$$

The requirement is that this  $\delta z$  must be greater than or equal to the thickness of the laser sheet to allow for errors in focussing over the entire flowfield. For the configuration used in these experiments,  $m=0.3$ , and the thickness of the laser sheer  $t$  is 1mm, thus the  $f^\#$  required of the camera lens is at least 5.0.

The next step in the PIV experimentation process is the measurement of displacements of many randomly positioned image pairs. In order to obtain velocities on a spatially well resolved basis, high density seeding is necessary. In the presence of many image pairs, statistical methods have to be used to determine an average displacement over a region. Many different methods have been developed to determine the the averaged displacement vectors in a chosen interrogation volume. A cross-correlation technique was used in this study to obtain the displacement vectors. Detailed description of the data analyses process is provided in the software section of this report.

### **3.1 LIGHT SCATTERING FROM PARTICLES**

The scattered intensity from a particle illuminated with light of intensity  $I_0$  is given by

$$I_s = I_0 \int_{\Omega} \frac{\lambda^2 \sigma \cdot \sigma^*}{4\pi^2} d\Omega \quad (3.9)$$

where  $\sigma$  is the Mie scattering coefficient of the particle (Kerker 1969). The ratio of the refractive index of the particle to that of the fluid is a significant parameter in light scattering. For scattering in water, the scattered intensity is at least 10 times smaller than particles scattered in air due to the difference in refractive index between water and air. In order to improve scattering efficiency, larger particles are used for illumination. Usually this is not a problem since the larger particles track flow in liquids without losing tracking fidelity. Mie scattering calculations for small particles (1-20  $\mu\text{m}$ ) can be used to estimate the strength of a particle image for various particle sizes, lens f-numbers, light sheet geometries, light pulse energies and detection medium sensitivity (Adrian and Yao, 1985).

The mean exposure on a detection medium averaged over the area of a particle image is given by

$$\bar{\epsilon} = \frac{\lambda^2 W \int |\sigma|^2 d\Omega}{\pi^3 (M^2 d_p^2 + 2.44^2 d_i^2 \lambda^2 / D_a^2) \Delta y_0 \Delta z_0} \approx \frac{\lambda^2 W d_p^n D_a^2}{\lambda^n d_0^2 (M^2 d_p^2 + 2.44^2 d_i^2 \lambda^2 / D_a^2) \Delta y_0 \Delta z_0} \quad (3.10)$$

where  $W$  is the energy of the light pulse,  $D_a$  the lens aperture diameter ( $f^\# = f/D_a$ ), and  $n$  is the power law exponent describing the scattered light energy. For small particles where the particle diameter is in the 1-10  $\mu\text{m}$  range,  $n$  is of order 3, and diffraction blurring dominates the denominator, the mean exposure can be approximated as

$$\bar{\epsilon} \approx W d_p^3 D_a^4 / d_0^2 d_i^2 \lambda^3 \Delta y_0 \Delta z_0 \quad (3.11)$$

This shows that the intensity drops rapidly with increased size of the system. The intensity also varies inversely as  $\lambda^3$  due to the combined effects of Mie scattering and diffraction spreading of the image into a spot whose area is proportional to  $\lambda^2$ .

### 3.2 RESOLUTION OF PARTICLE MOTION

The accuracy of velocity measurements is determined by the ability to accurately calculate displacements from the PIV data. Assuming  $\Delta x$  is the actual displacement and  $\Delta X$  is the projection of the displacement on the image,

$$\Delta X = M\Delta x = Mu\Delta t \quad (3.12)$$

and

$$\frac{\sigma_u^2}{u^2} = \frac{\sigma_{\Delta x}^2}{\Delta x^2} + \frac{\sigma_{\Delta t}^2}{\Delta t^2} \quad (3.13)$$

where  $\sigma^2$  denotes the mean square value of the error in measuring the subscript quantity.

The uncertainty in  $\Delta x$  rises from errors in locating the appropriate reference points on the particle images used to mark the beginning and end of the displacement. These errors may arise from shape irregularities, finite resolution due to recording, finite pixel size and noise in the camera readout.

$$\sigma_{\Delta x} = c \left( d_r + M\sqrt{u^2 + v^2} \delta t \right) \quad (3.14)$$

The uncertainty in  $\Delta t$  depends on the light source and the circuitry used to generate the time delay between the two pulses.

## 4. INSTRUMENTATION DEVELOPMENT

In the first four quarters of this program, efforts were concentrated on developing the necessary instrumentation for a two color particle imaging velocimetry system. The basic requirement of the two-color system was the ability to perform experiments in a supersonic flowfield with velocities in excess of 500 m/sec and in the presence of particulates and two phase flow medium. These high speeds and complex flowfield require that the time separation between the two laser

pulses be in the sub microsecond range, high resolution and the capability to resolve directional ambiguity in the flowfield. Although double pulse single laser systems are currently available, pulse separations below 1  $\mu$ sec are not available. Currently, commercially available PIV systems use pulsed and continuous wave lasers depending on the application requirements. Pulsed lasers are typically used for performing flow measurements in air, due to the higher velocities that can be attained. Continuous wave lasers along with optical choppers are used in systems where the velocities are typically less than 1 m/sec. Also, the single pulsed laser systems are limited in the lower range of time separations by the delay time in the Nd:YAG laser Q-switch. Thus, in order to devise a PIV system suitable for supersonic and subsonic applications, two pulsed lasers are required with independent control of the pulse separation through each laser.

#### **4.1 OVERALL PIV SYSTEM**

The overall PIV system consists of several different elements. Figure 1 is a block diagram of a typical PIV system. The system consists of the lasers and the supporting optics which constitute the beam delivery system, the electronics which are used to synchronize and set the time delay between the beam pulse delivery and the image capture process, and the image capturing system. Each of these units were carefully chosen to make the system portable and usable over a wide range of flow conditions. In addition, the overall system requires a computer for image storage and subsequent processing. The individual elements of this overall system will now be discussed in detail.

##### **4.1.1 LASERS**

Two Continuum Surelite I lasers (Serial Numbers 2096A, 449 PS and 2523, 2523) were chosen for the PIV system. The lasers operate at a repetition rate of 10 Hz and have a rated output of 200 mJ/pulse at 532 nm (second harmonic), which is one of the wavelengths required for the two-color PIV system. The lasers consisted of the

primary Nd:YAG oscillator rod which produced  $1.06\text{ }\mu\text{m}$  radiation. Typically the Surelite lasers produced 500 mJ of output at the primary wavelength with a pulse

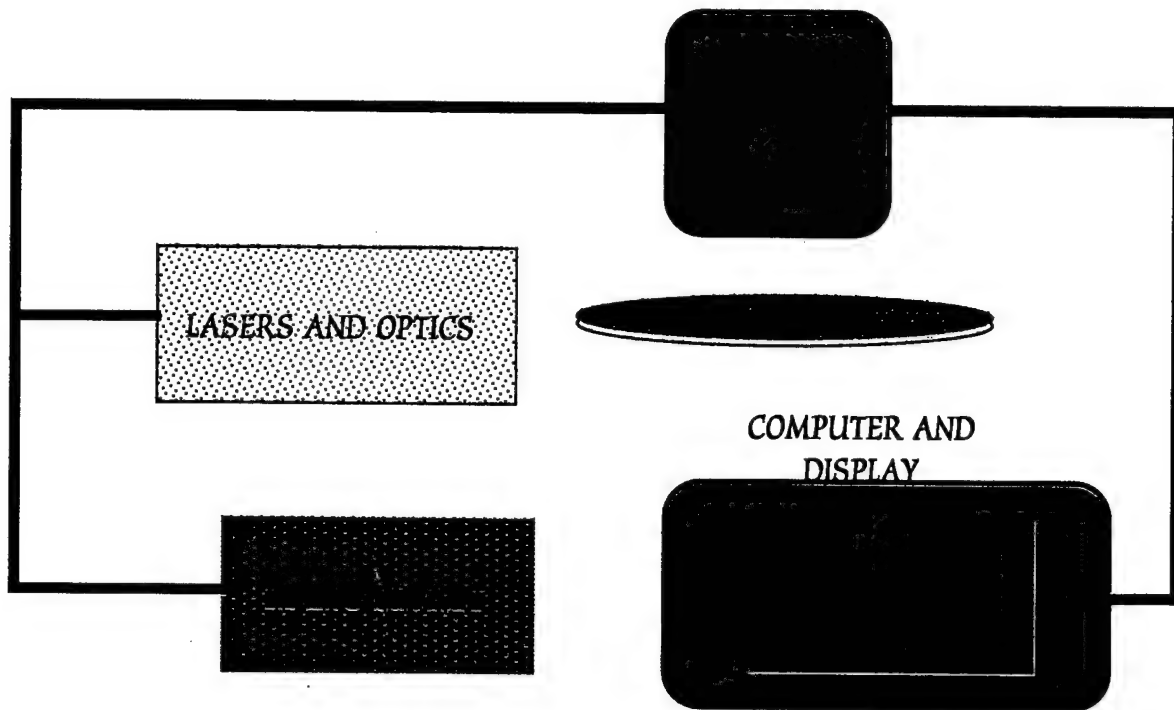


Figure 1. Block Diagram of a Typical Particle Imaging Velocimetry System.

duration of 8 nsecs. The primary output is frequency doubled with a Q-switch to produce 532 nm irradiation. The 532 nm beam from one of the lasers provided one of the two wavelengths required for the two color PIV system. Two separate lasers were used instead of a single double pulsed laser because the delay times required were less than 1  $\mu\text{sec}$ , which is not currently available with double pulsed laser systems. The typical beam diameter out of the laser was 6 mm. These continuum lasers were chosen due to their compact packaging, high output, low cost and simplicity of operation. The beam quality produced by the Surelite I laser was uniform and contained no hot spots. Prior to alignment of the PIV system and running the PIV experiments, the lasers were left running to stabilize the output power and the beam quality.

#### 4.1.2 RAMAN CELL

In order to produce the second color for the PIV system, a Raman cell was utilized. The Raman cell consists of a 1 meter long stainless steel tube which is filled with the chosen gaseous medium, which converts the incident 532 nm light into 607 nm light using Raman (inelastic light) scattering. Figure 2 shows a schematic of a Raman cell setup. The cell consists of a hollow stainless steel cylinder 1 meter long and 2.54 cm internal diameter. The two ends of the cylinder are fitted

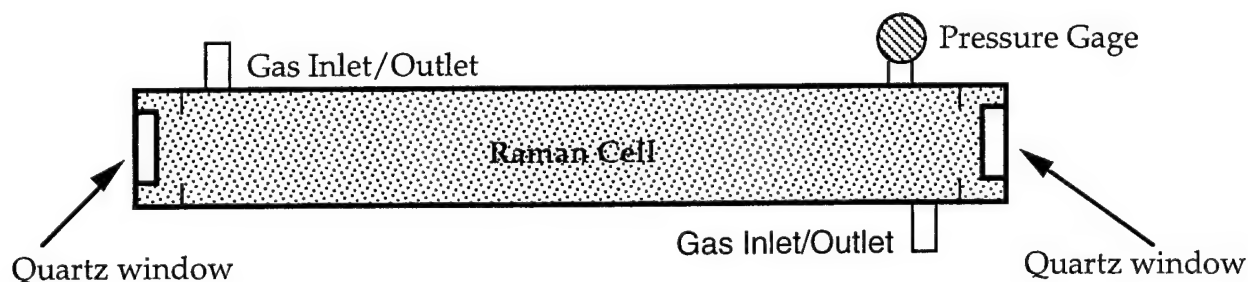


Figure 2. Schematic of Raman Cell Used in the Two-Color PIV System

with optical windows. The cylinder is typically pressurized to 1000 psi with the gas which produces the desired wavelength. In the experiments described in this report, the cell was filled with nitrogen which produced the shift to 607 nm. The Raman cell was purchased from Princeton Optics, Inc. Initial experiments showed a conversion efficiency of 32% with a saturation point reached at input energy levels of 110 mJ/pulse. In order to obtain higher outputs from the Raman cell, it was fitted with AR coated mirrors, so that the losses incurred at the 4 window surfaces could be minimized.

#### 4.1.3 OPTICS

Since both the wavelengths utilized visible wavelengths, the optics chosen for directing the beams and forming the interrogation sheet were anti-reflection coated in the visible 400 - 700 nm region. Optics were chosen to have high damage thresholds so that damage to the optics during regular operation could be minimized. The essential parts of the optics consisted of beam turning mirrors and prisms, a dichroic beam splitter/combiner for combining the two wavelengths for

PIV, and the cylindrical and spherical optics which were used to generate the light sheet. The Raman cell required some special consideration in order to obtain the highest efficiency output and yet preserving the integrity of the cell. As described above, the Raman cell is fitted with an input and an output window for the beam. A 750 mm focal length focussing lens is used to focus the 532 nm radiation into the Raman cell so that the beam is focussed within the first half of the Raman cell. The output beam from the Raman cell consists of both the incident wavelength light and the Raman shifted radiation. The light exiting from the Raman cell is collimated using a second 750 mm focal length lens and then passed through the beam separation and sheet forming optics.

The dichroic beam splitter is used direct the red and the green beams in a colinear manner on to the sheet forming optics. The output from the Raman cell is passed through a color glass filter to remove the remnant incident green light. The two colinear beams are then then directed through a set of prisms onto a different vertical plane for introduction into the test section. Figure 3 shows a schematic of the optics box assembly developed to generate the collimated optical sheet. The box consists of an input end which houses a variable ratio beam expander, which is used to expand the sizes of the two beams so that the intensity distribution throughout the extent of the beam is smooth. The exiting beam diameter is adjusted so that the beams are roughly 1 inch in diameter.

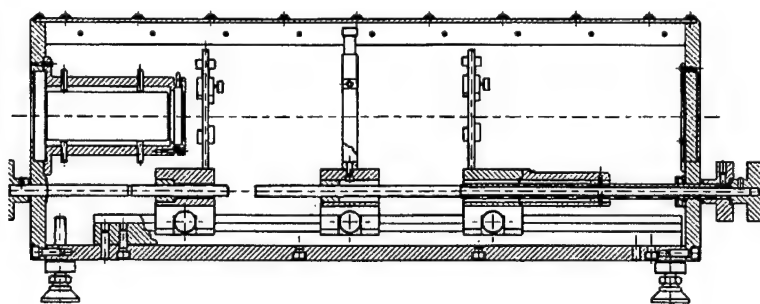


Figure 3. Schematic of the Optics Box Disgned to Generate the Laser Sheet.

The next stage of the beam delivery process is the generation of the optical sheet. This is performed by passing the expanded beam through a combination of cylindrical and spherical lenses. The optics box schematic shown in Figure 3 offers the flexibility of changing the sheet width without changing the optical components. The sheet width can be altered by changing the axial spacing between the cylindrical and spherical lenses. The focal length of the optics used was determined by the location of the wind tunnel test section and the placement of the PIV system. Typically a negative cylindrical lens (focal length 150 mm) was used with a 3 inch diameter spherical lens (focal length 200 mm). A second negative lens is used in the crossed configuration to collimate the sheet. The thickness of the sheet is then defined by the wavelengths of radiation and the f-number of the lenses used.

Figure 4a shows a schematic of the overall PIV system developed during this Phase II program. The system is portable and the optical parts are situated on a

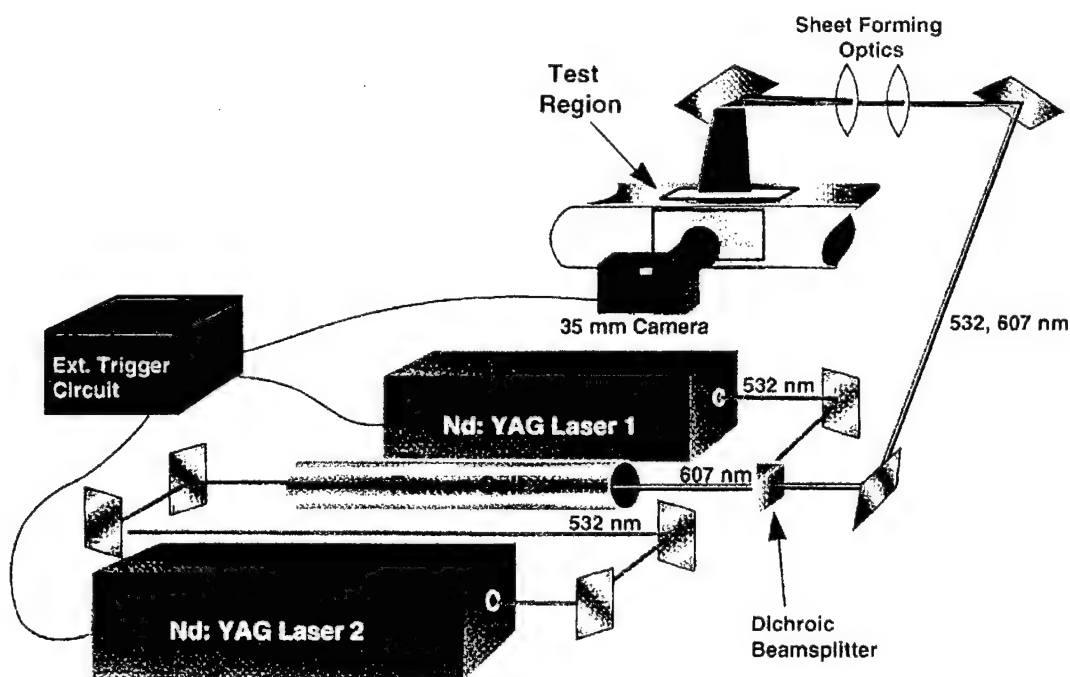


Figure 4a. Schematic of Two Color PIV System

movable bi-level optical bench. The lasers, the Raman cell and the beam steering optics are located on the upper shelf and the sheet forming optics are located on the lower shelf in the arrangement shown (Figure 4b). The arrangement is



interchangeable in case the optical sheet is required to be delivered at a lower level. All of the sheet forming optics are housed in a compact enclosure in order to make the system modular in nature. The entire PIV system is assembled on a movable optical bench so that the system can be transported between facilities and setup time is minimized. Experiments have typically been performed with the sheet width

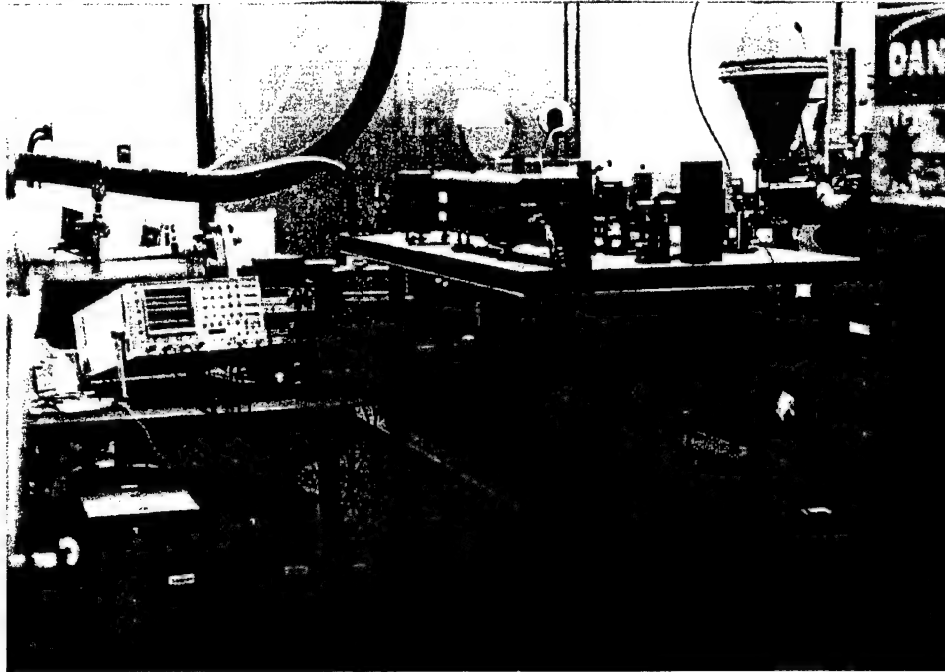


Figure 4b. Photograph of Two Color PIV System.

varied between 1.5 inches and 2.5 inches. The optical energy incident at the test section is estimated to be between 12 and 15 mJ. The width of the collimated sheet at the test section was estimated to be around 0.75 mm.

The red and green beams are combined by a dichroic beam splitter and directed through a series of spherical and cylindrical optics to generate a sheet with a thickness of  $< 1\text{ mm}$  at the test section. The width and the thickness of the laser sheet can be varied depending on the needs of the experiments. The measured outputs out of the lasers are 100 mJ/pulse for the beam that pumps the Raman cell, and 50 mJ/pulse for the 532 nm beam. The energies of the two beams were equalized at the test section to avoid bleed through and saturation effects on the captured images.

This procedure is generally performed by visual estimation. The temporal delay between the two lasers is controlled by a pulse generator and is set as a function of the gas velocity, interrogation spot size, and optical magnification ( $m$ ), where  $m$  is defined as the dimension of an objects projection onto the image plane. In the experiments with the digital camera, the delay timing was set at 300 ns, whereas for the experiments with the 35-mm camera, the timing was set at 220 nsec.

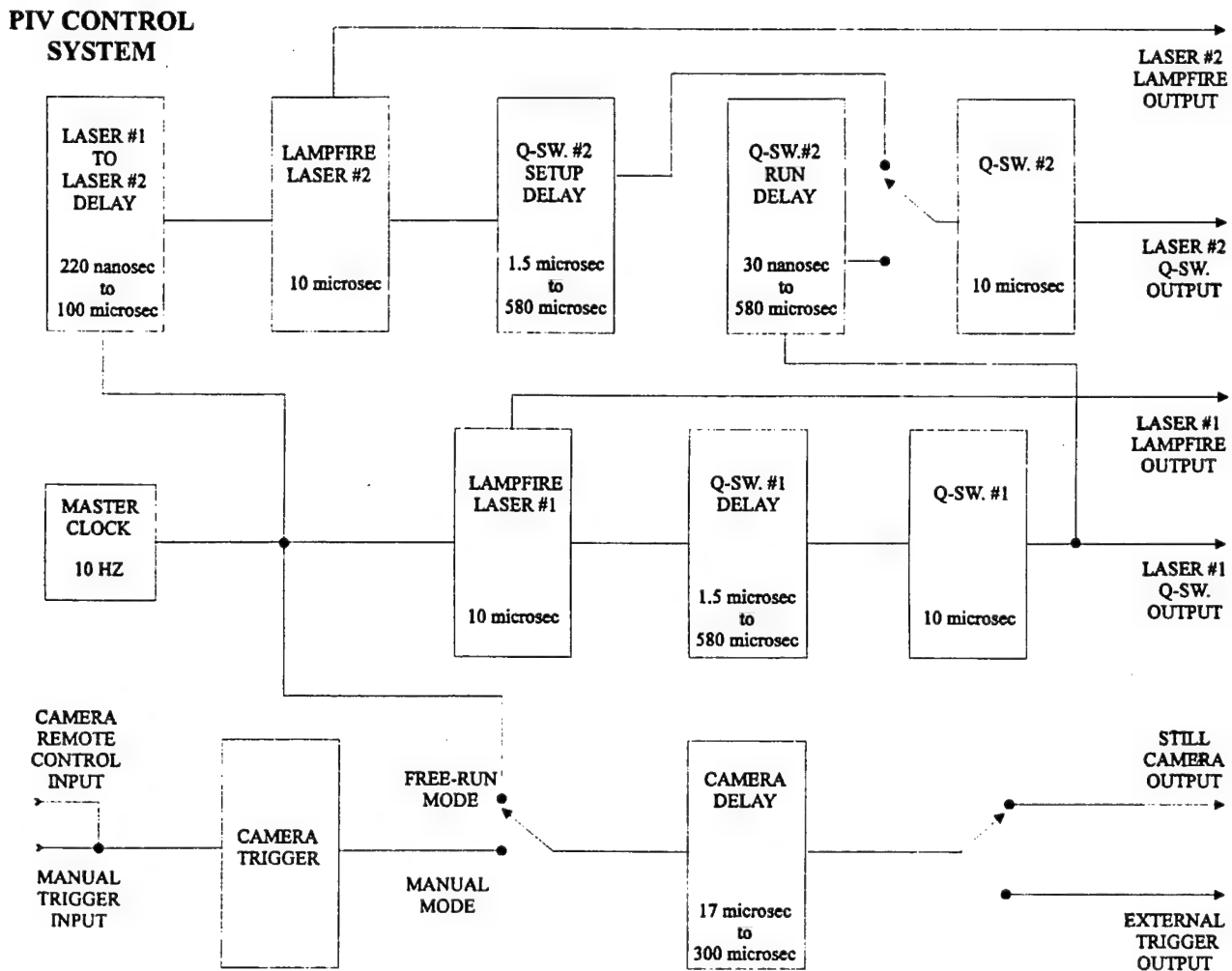
#### **4.2 TIME DELAY ADJUSTMENT**

The timing between the pulses can be adjusted depending on the flow velocities under investigation. The two color image of the seeded flowfield is then captured using an image capture medium, such as a 35 mm camera, a digital color camera or an 8 mm video camera. Knowing the resolution of the digitized image, and the timing separation between the two pulses, flow velocities for a chosen interrogation volume which contains at least one particle pair can be calculated in a two-dimensional image. The timing separation between the two laser pulses was obtained by using the custom made timing control circuit box. The timing circuit box was connected to the lamp fire control and the Q-switch control for both the lasers. The lasers typically operate with a preset delay between the lamp fire and the Q-switch. The time between the pulses is adjusted by adjusting this delay between the lamp fire and the Q-switch activation.

Figure 5 is a block diagram of the laser and camera timing control circuit. Delay times as low as 0.2  $\mu$ secs or up to 1 second can be generated using the circuit. Figure 6 shows a photograph of the timing circuit unit. The unit was designed to be modular so that the unit became a stand alone product which could be used for many different applications. Initial experiments showed that there was some jitter generated by the circuit (about 30 nsec.). For supersonic PIV experiments this jitter was significant since the typical delay times were around 300 nsec. Thus the jitter contributed to 10% uncertainty in the supersonic velocity measurements. This was subsequently corrected by using electronic parts with better tolerances. In the most

recent experiments performed with the PIV system, the jitter was estimated to be less than 2 nsec.

The circuit enables the external triggering of the lasers and the triggering of the camera so that the double pulsed, two color images can be captured by the camera



12/30/96 B.T.

Figure 5. Block Diagram of Laser Timing Control Circuit.

system. The two still cameras used in the experiments described here were triggered using the same circuitry. The camera shutter speed is preset and the delays are adjusted so that one image is captured on each frame. The trigger pulse for the

camera is synchronized with the trigger pulses for the two lasers so that instantaneous shots of the experimental field can be obtained. In order to perform the experiments with the 8-mm video camera, the lasers were synchronized to the 16 Hz rate at which the video camera operated. This was performed by operating the lasers at 8 Hz and then by changing the delay using the timing circuit so that the video camera was synchronized with the two lasers. The detailed documentation for the circuitry is attached in the Appendix.

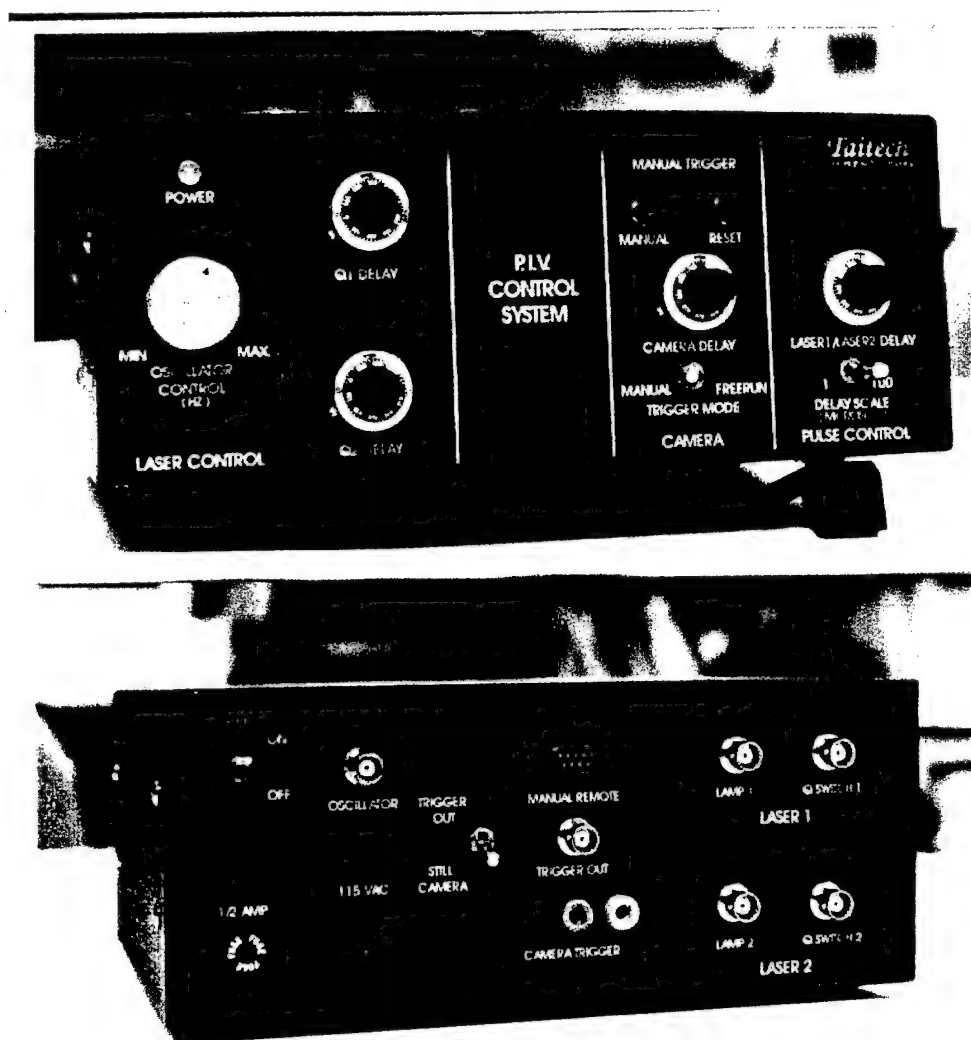


Figure 6. Photograph of the Laser Timing Control Circuit.

### 4.3 IMAGE ACQUISITION SYSTEMS

The PIV images were captured using 3 different types of media. Images were captured using a standard 35 mm film camera, a Kodak DCS 460 color digital camera and a Sony 8mm video camera. The images taken with the 35 mm camera provided the finest resolution, however, the post processing of the images was time consuming since each of the images had to be digitized. Images that were acquired with the 35 mm film camera were first developed and then digitized using a Polaroid Sprintsan scanning system. The digitized images were then stored as PICT files for subsequent image processing. The images were scanned in at the highest resolution available with the scanner, i.e. 2800 dpi. This resulted in a single file being 23MB. In addition, the scanning process is quite time consuming. Typically 1 roll of 36 exposure film took 6 hours to digitize. The digital camera enabled us to speed up the data collection and obtain feedback during experimentation so that experimental parameters could be optimized.

The Kodak DCS 460 digital camera provided the most convenient alternative. The results of the experiments could be viewed immediately following the imaging process so that experimental parameters could be suitably adjusted. This CCD sensor has a resolution of  $3060 \times 2036$  pixels, and each pixel is 9-mm square. The CCD camera has a built-in 12-bit analog-to-digital converter for increased dynamic range and a frame rate of 1 frame/sec. It also features a PC-MCIA storage drive that delivers ~ 26 exposures, with each PIV image occupying 18 Mbytes. Only three to four images were obtained during each 25 seconds of tunnel operation because of the time required for the camera to reset after the first two images. A 105-mm micro lens with an f-number of 5.6 was used to record the 0.69-magnification images. A 2x extension ring was added to the lens to achieve the 1.92 magnification. A recent study has proven that the proprietary interpolation software developed by Kodak is effective in maintaining the equal red, green, and blue pixel spatial resolution required for accurate PIV measurements, despite unequal pixel color distribution.

An 8 mm video camera was also used to demonstrate the use of the PIV technique with a video camera and a frame grabber. The use of the video camera provides a reduced cost alternative to the digital camera for acquiring large volumes of data in addition to providing an avenue to perform time resolved measurements. Typical 8 mm video cameras are usually equipped with a 578 x 356 CCD chip, which means that the resolution obtained through the camera alone is limited. In order to extend the resolution limit, external lenses were used to obtain a magnified image of the viewing area.

#### **4.4 CAMERA INTERFACE**

The major limitation in high resolution two color PIV experiments performed with a digital camera is the storage capacity available for the images. During the actual runs, the images are stored on a storage card fitted in the digital camera which is capable of temporarily storing 25 images. Each of the compressed image files are 6 megabytes in size. Once the storage card is full, the tunnel run was halted to transfer the images on to the computer hard disk. The computer used for these experiments was a Macintosh 9500 200 MHz Power PC (Serial No. XB63907X8L7\*). A 21" Hitachi color monitor was used to view the images during and following the data acquisition. The computer is equipped with a 2 gigabyte hard drive and 64 megabytes of RAM in order to hasten the normally time consuming image processing functions. The computer also is equipped with built in Audio-Video (AV) and frame grabbing capability. This feature in the computer is essential for interfacing with the video camera.

The Kodak digital camera control was performed through a plug-in module for the well-established Adobe Photoshop software. The Photoshop software was also used to display, store and manipulate the acquired images. The Photoshop software was used to run the film scanner and digitizer so that digitized versions of 35 mm film images could be created. The limited number of image sets is thus a direct consequence of the large file sizes and the limited amount of data storage space

available. Typically for each day of running, 1.5 gigabytes of storage space was utilized. Prior to the next run, the hard disk was downloaded into portable Iomega Zip disks. The data on the Zip disks was then archived using a CD recorder. The image analysis procedure was also performed with the same computer.

## 5. ANALYSIS SOFTWARE

The software used to process the digitized images was also developed by Taitech, Inc. The software performs a cross-correlation (2D FFT) analysis on a single two color PIV image so that correlation (displacement) vectors are identified. Typically, the whole image was divided into interrogation areas which were chosen depending on the resolution requirements for the data. The correlation peaks are identified and then selected following comparison with the peaks in the neighboring interrogation areas. This particular scheme allowed us to obtain errors in the sub pixel range which will be demonstrated later in the report. Vector removal and vector interpolation are then performed by the analysis program to complete the process. The process sequence of the correlation calculations is similar to the one outlined by Tennekes and Lumley[1972].

### 5.1 THEORY OF DIGITAL PIV (DPIV)

DPIV is basically a determination of cross correlations between sub regions of successive images (Sholl and Savas 1997). Consider images  $I(x,y,t)$  and  $I(x,y,t+\delta t)$  of a thin slice of the flowfield seeded with particles of diameter  $d_x$  and illuminated with a laser sheet of thickness  $\delta z_0$ . Assume that the subregions  $f(x,y) \subset I(x,y,t)$  and  $g(x,y) \subset I(x,y,t+\delta t)$ . The cross-correlation  $h(x,y)$  of the two subregions  $f$  and  $g$  can be written as

$$h(x,y) = \iint f(x+\xi, y+\eta)g(\xi,\eta)d\xi d\eta \quad (5.1)$$

The location of the peak of  $h(x,y)$  corresponds to particle distribution displacement between the regions bounded by  $f(x,y)$  and  $g(x,y)$ . The components of the velocity gradient tensor  $u_{ij}$  is given by

$$u_{ij} = \frac{\partial u_i}{\partial x_j} = e_{ij} + \frac{1}{2} r_{ij} \quad (5.2)$$

where the symmetric component strain rate tensor is given by  $e_{ij} = \frac{1}{2} \left( \frac{\partial u_i}{\partial x_j} + \frac{\partial u_j}{\partial x_i} \right)$  and

the antisymmetric component rotation sensor is  $r_{ij} = \left( \frac{\partial u_i}{\partial x_j} - \frac{\partial u_j}{\partial x_i} \right)$ . The correlation

peaks correspond to the mean velocity in the region  $f$ . As the values in  $u_{ij}$  increase, the height of the correlation peak decreases and its width increases. There are many factors which contribute to the width increase and height reduction of the correlation peak thus reducing the accuracy of the velocity measurements. Some of these factors are optical misalignment, out of plane motion, in plane motion and deformation of the particle distribution due to local flow variations  $u_{ij}$ .

The need to study velocity fields is necessitated by flowfields in which the velocity gradient tensor  $u_{ij}$  is non zero. Non zero  $u_{ij}$  components degrade the accuracy of most flow measurements including PIV. PIV is found to bias towards low speed particles in a correlation region. This is due to the fact that image overlap and thus the local weight of particles in the cross correlation  $h$  decreases with increasing velocity. This bias can be controlled by limiting the displacement. Also, there is an effective reduction of the correlation region due to large velocity gradients.

The autocorrelation of a two variable Gaussian is given by



$$A(\lambda) = \int_{-\infty}^{\infty} e^{ar^2} e^{-a(r-\lambda)^2} dr \quad (5.3)$$

which can be determined by a Fourier transform as

$$A(\lambda) = \frac{\sigma\sqrt{2}}{2} e^{-\frac{\lambda^2}{4\sigma^2}} \quad (5.4)$$

For a circular correlation region of radius  $R$  filled with particles of illumination intensity  $I_0$ , Gaussian radii  $\sigma$  and a particle density of  $D = N_{\text{particles}} / A_R$  where  $A_R$  is the correlation region area  $\pi R^2$ . The maximum peak height can then be calculated as

$$h_{\text{max}} = \sigma I_0^2 \pi R^2 D \sqrt{2} / 2 \quad (5.5)$$

Vorticity  $\omega$  reduces this height due to the reduced correlation between particles in the two regions. The reduced correlation peak height  $h(\omega t)$  is given by

$$h(\omega t) = \int_0^{2\pi R} \int_0^2 I_0^2 r D \sigma \frac{\sqrt{2}}{2} \left( e^{-bR^2} \right) r dr d\theta = \sigma I_0^2 \frac{\sqrt{2}}{2} \frac{\pi D}{b} \left( 1 - e^{-bR^2} \right) \quad (5.6)$$

where

$$b = \left( \frac{\omega t}{2} \right)^2 / (2\sigma^2) \quad (5.7)$$

The dependence on area is determined by checking the expression in the limit  $\omega t$  approaches zero.

$$\lim_{b \rightarrow 0} \frac{1 - e^{-br^2}}{b} = R^2 \quad (5.8)$$

$$\lim_{\omega t \rightarrow 0} h(\omega t) = \sigma I_0^2 \pi R^2 D \sqrt{2} / 2 \quad (5.9)$$

A relationship between the vorticity and the maximum correlation peak height may be defined by the reduced peak fraction which is given by

$$K = \frac{h(\omega t, R)}{h_{\max}} = \frac{1 - e^{-bR^2}}{bR^2} = \frac{1 - e^{-\left(\frac{\omega t}{4\sigma} R\right)^2}}{\left(\frac{\omega t}{4\sigma}\right)^2 R^2} \quad (5.10)$$

The software method developed during this program, improved displacement correlations by incorporating the notion of fractional displacement. Once a crude estimate of the local displacement is obtained, an analysis was performed of the surrounding pixels to obtain sub-pixel displacement. The fractional displacement estimator was formulated as follows:

At a local maximum of the natural logarithm  $\ell$  of an intensity distribution  $I$  we have

$$\nabla \ell(x, y) = 0$$

Expanding in a Taylor series about the point  $(x, y)$  we have

$$\nabla \ell(x + \varepsilon_x, y + \varepsilon_y) = \nabla \ell(x, y) + \left( \varepsilon_x \frac{\partial}{\partial x} + \varepsilon_y \frac{\partial}{\partial y} \right) \nabla \ell(x, y) + \frac{1}{2!} \left( \varepsilon_x \frac{\partial}{\partial x} + \varepsilon_y \frac{\partial}{\partial y} \right)^2 \nabla \ell(x, y) + \dots \quad (5.11)$$

eliminating terms higher than the first order in the displacements and applying the condition for maximum we have

$$\nabla \ell + \varepsilon_x \frac{\partial \nabla \ell}{\partial x} + \varepsilon_y \frac{\partial \nabla \ell}{\partial y} = 0 \quad (5.12)$$

$$\frac{\partial^2 \ell}{\partial x^2} \varepsilon_x + \frac{\partial^2 \ell}{\partial x \partial y} \varepsilon_y = -\frac{\partial \ell}{\partial x} \quad (5.13)$$

$$\frac{\partial^2 \ell}{\partial x \partial y} \varepsilon_x + \frac{\partial^2 \ell}{\partial y^2} \varepsilon_y = -\frac{\partial \ell}{\partial y} \quad (5.14)$$

The subpixel displacements can be calculated from this set of equations.

## 5.2 ANALYSIS PROCEDURE

Figure 7 described the overall data analyses process. The image analysis process consists of four steps. First, the digitized image which is typically 3000 x 2000 pixels is divided into 12 equal areas for ease of viewing. The processing is performed on each of these areas sequentially until the entire image is analyzed. Each viewing area on the screen is then divided into interrogation areas which are determined by the resolution required. A 2D Fast Fourier Transform (FFT) map is calculated to determine the correlation map for the two color image. Since two colors are used in the imaging process, and the leading beam color is preset, directional ambiguity is

automatically removed from the data. The resultant correlation map shows two spots, the center being the correlation of the first spot on to itself and color leakage, and the second spot which is the cross correlated peak. The vector defined by the two spots as shown in the figure is the calculated displacement vector. As can be seen from the correlation map, the result is non-symmetric and hence void of directional ambiguity. The second step identifies the peaks and forms the raw displacement vector field for the processed area. This is followed by a step which removes "bad vectors" using a two part process. In the first pass, range determination is carried out followed by a comparison of the calculated displacement to displacement values of neighboring vectors. The software also possesses the capability of removing the bad vectors interactively. The final step is a 2D interpolation scheme for vector preservation. The software is written in FORTRAN which makes it portable to high end number crunching computers and UNIX systems.

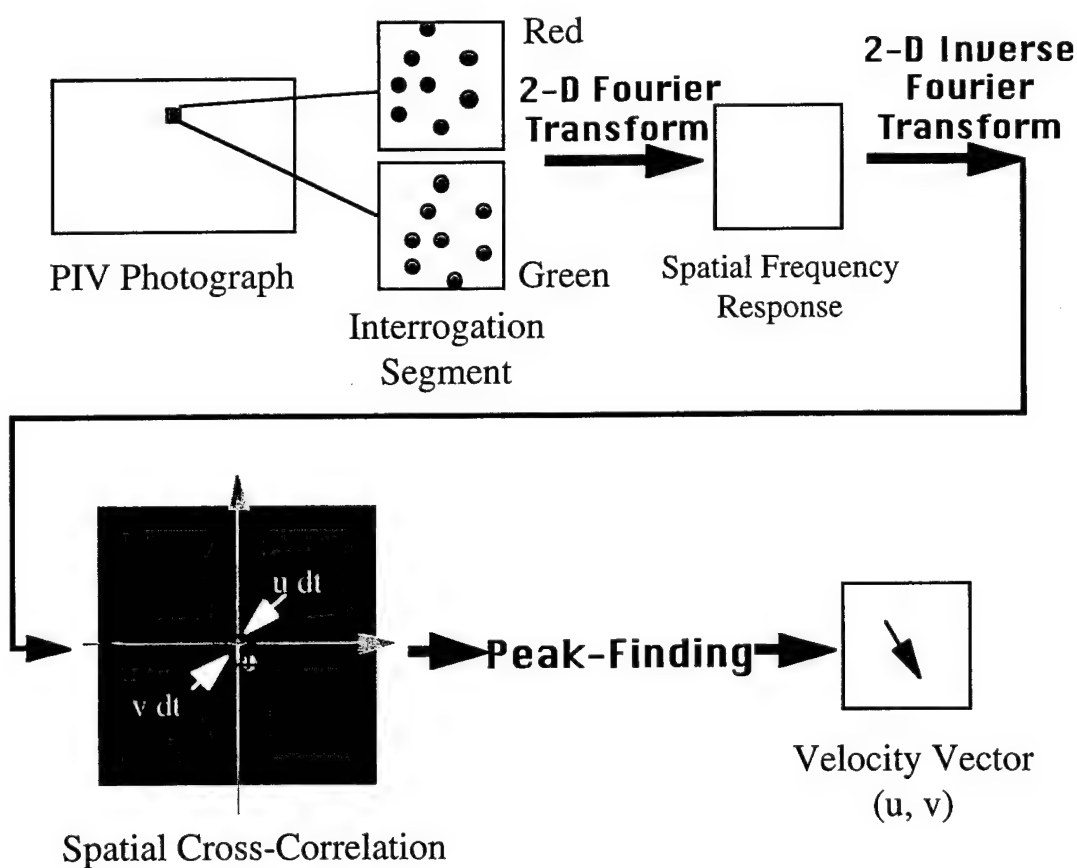


Figure 7. A schematic representation of the PIV Analysis Software.

The displacement for the particular image is dependent on the image resolution and the timing separation between the red and the green light illuminated particles. In order to determine the particle displacement, a cross-correlation method is used to compute a 2D Fast Fourier Transform (FFT) of the image. FFT's in  $128 \times 128$ ,  $64 \times 64$ , and  $32 \times 32$  pixel units can be calculated for each of the images. The FFT procedure identifies correlation peaks for each of the unit areas, which denote the most probable displacement vector for each location. There are several optimization schemes built into this method in order to correctly identify the vector location. In most instances, three correlation peaks are identified and then the peak identity is determined through a second order correlation with the neighboring vector locations. A demonstration of the results obtained through the overall PIV experimentation process will be described in detail in the experimental validation portion of the report.

A flow diagram of the functionality of the PIV software is shown in Figure 8. In order to perform the cross-correlation analysis the red and green portions of the two color PIV image were separated into two distinct sets of data. The PICT file format was chosen to handle the color information efficiently in a Macintosh computer system, although the "raw" image files generated through the Kodak 460 digital camera can also be used to analyze the PIV data. Since the analysis software is coded in FORTRAN, the software can be readily transported on to a PC or a workstation platform. The software as it runs on the Macintosh Power PC platform is menu driven and utilizes the Graphics User Interface available on Macintosh. A listing of the code is provided in the Appendix.

The software runs on a Macintosh Power PC platform although the code can easily be transported to other computing platforms such as an IBM system or a UNIX workstation. The software is user friendly, menu driven and utilizes the graphics capabilities of a Macintosh computer. The software calculates the correlation vectors between the red and the green particles within a set image area

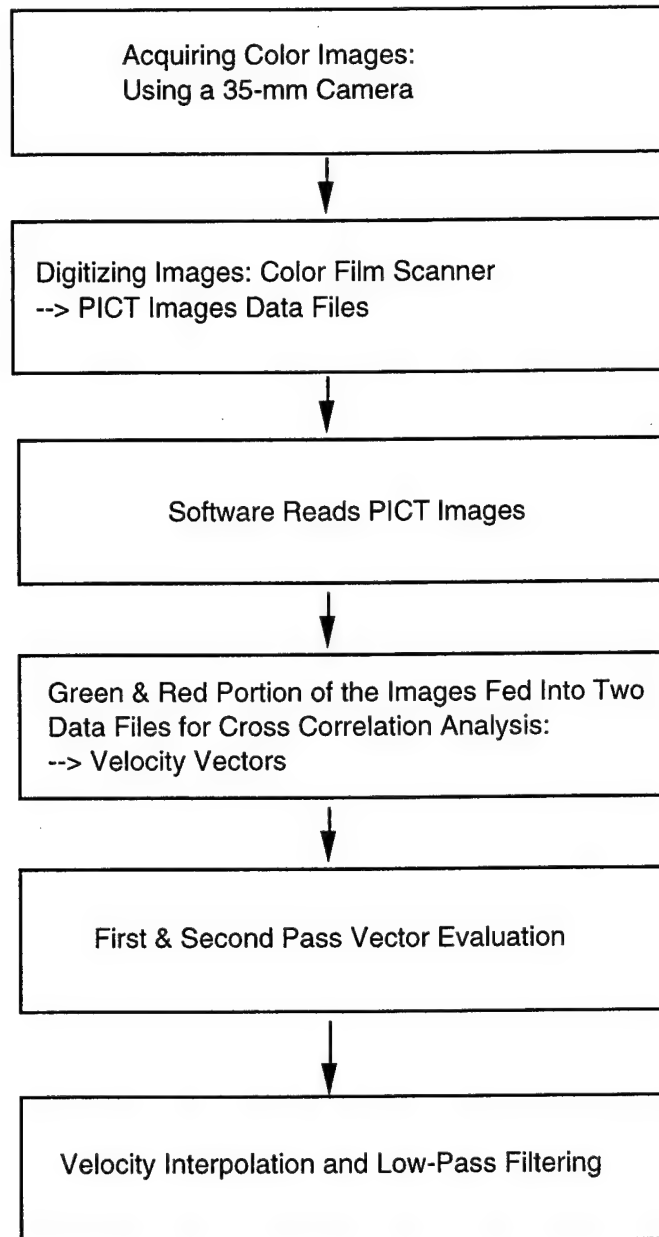


Figure 8. Flow Diagram for the PIV Data Analysis Software.

through 2D FFT analysis. A three level peak finding routine is used to identify the peak with sub pixel resolution. Figure 9 shows an image of the computer screen during the PIV data analysis process. The white arrows shown are the displacement vectors which are calculated for each interrogation area chosen. The interrogation area can be chosen in  $32 \times 32$ ,  $64 \times 64$ , or  $128 \times 128$  pixel units depending on the

resolution desired. In addition to processing individual image files separately, the program can also execute batch mode operations when several files are to be similarly processed. This mode is typically used when several images for a given condition have to be processed and the resulting data are to be used for calculating statistical ensembles for the set of images. All of the statistical calculations reported here were performed by running the program in batch mode with the same set of input parameters for a given image group.

### **5.3 SOFTWARE TESTING**

The newly developed software was first tested on 2-color PIV images taken of a rotating wheel which was used to simulate vortex motion. Double pulsed PIV images were acquired with a 35 mm camera with the red laser beam pulse followed by the green laser beam pulse. Once the images were acquired, the film was developed and the negatives digitized with a digitizing film scanner and then stored

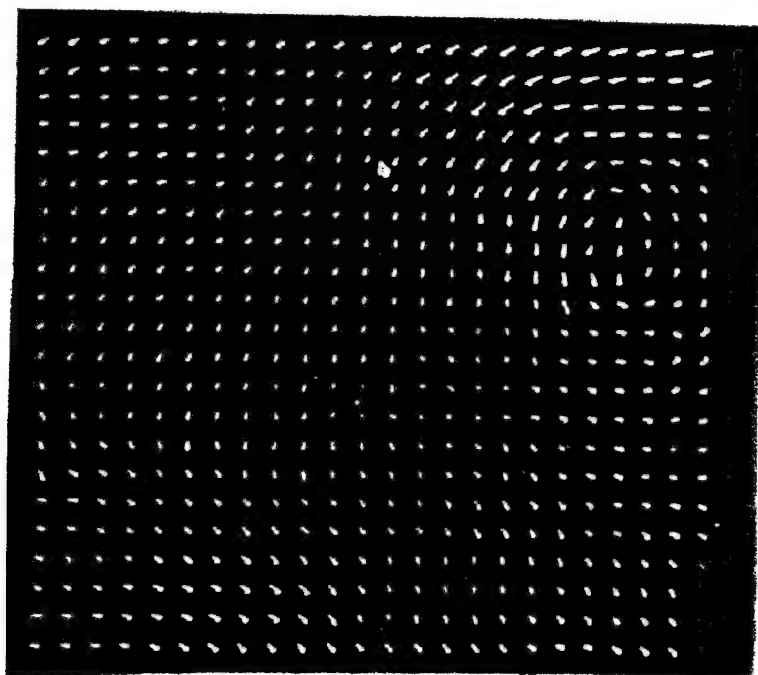


Figure 9. Image of Computer Screen During PIV Image Analysis.

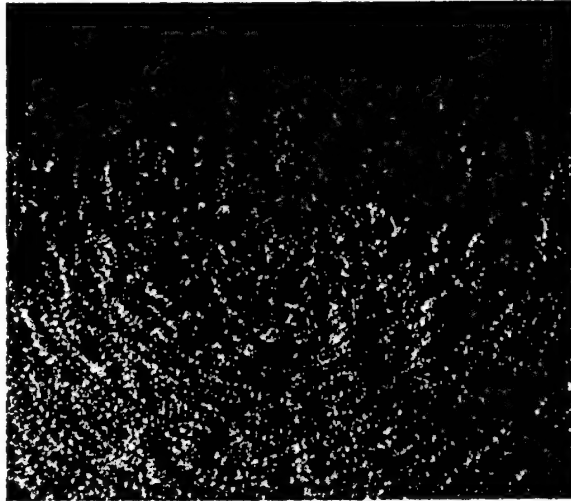


Figure 10. Digitized Two Color PIV Image of Test Wheel.

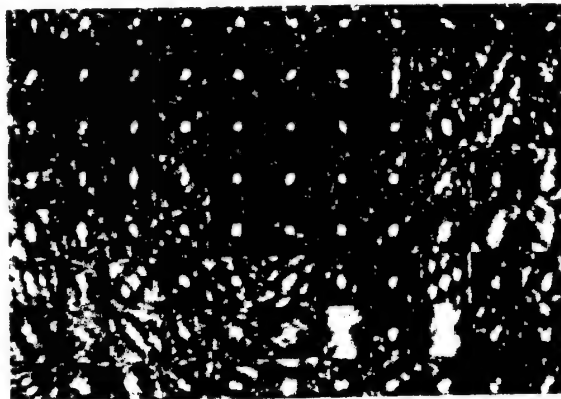


Figure 11. Computer Screen Image of FFT Correlation Map for the Wheel Image.

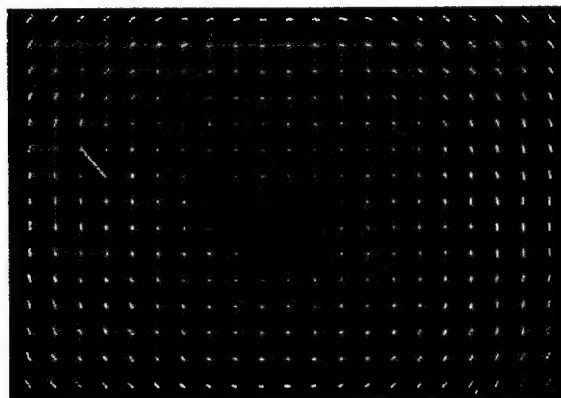


Figure 12. 2D Vector Displacement Plot Calculated for the Image in Figure 10.



in PICT file format. The image plane was divided into  $64 \times 64$  pixel units. The resulting correlation map for each unit was then used for peak searching. Figure 10 is a digitized image acquired using the rotating wheel and the two color PIV system. Figure 11 shows a computer screen image of the correlation map performed on the image shown in Figure 10. Figure 12 shows a plot of the instantaneous two dimensional velocity map for the same image. The plot shows that the velocity of the particles near the center of the wheel is near zero and largest at the outer edges of the wheel as expected.

An 8-mm video camera was used to acquire two color, double pulsed images from the rotating wheel. The video was then fed into the video input port of a Macintosh PowerPC 8500. The grabbed image was then stored as a PICT file for processing. Figure 13a shows a two-color double pulsed image obtained from the rotating wheel using an 8-mm video camera. The resolution of the image is

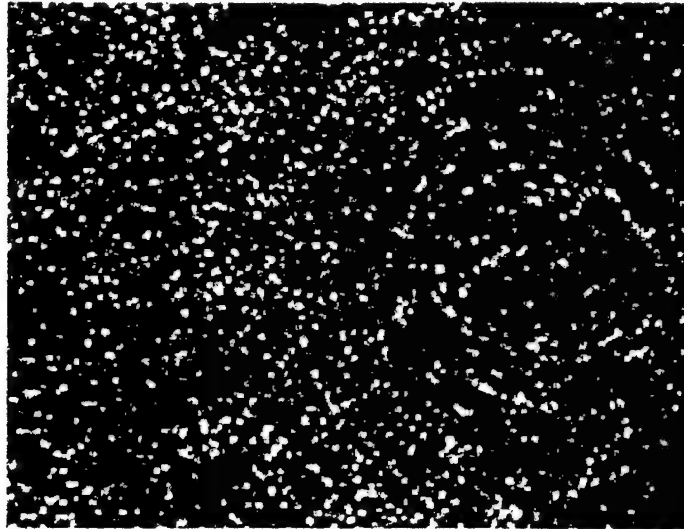


Figure 13a. Two Color Double Pulsed Image with an 8 mm Video Camera.

currently limited by the resolution of the camera. A correlation map was made from the image data, and the results used to map a vector plot. Figure 13b shows a vector

plot of the raw data. The length of the vector is proportional to the velocity at the given location. The velocity is calculated knowing the resolution of the digitized image and the time delay between the pulses.

The image shows the general trend for the circular motion of the wheel, but shows many vectors that do not correlate with the overall motion. An interactive "bad vector" removal procedure is then performed through the analysis software. The resulting data is used to make a new vector plot. Figure 13c shows a vector plot of the data following the removal of the "bad vectors". The plot shows areas where there are no vectors displayed. An interpolation routine is then performed to obtain the final version of the vector plot. Figure 13d shows a plot of the digitized image of the wheel following the interpolation procedure. The resulting data shows the gradual increase in the wheel speed from the center of the wheel moving outward. Currently efforts are being made to improve the resolution of the images obtained with the video camera by using an additional focussing lens along with the video camera so that a small region can be probed with high resolution. Data taken using this improved arrangement is currently being processed.

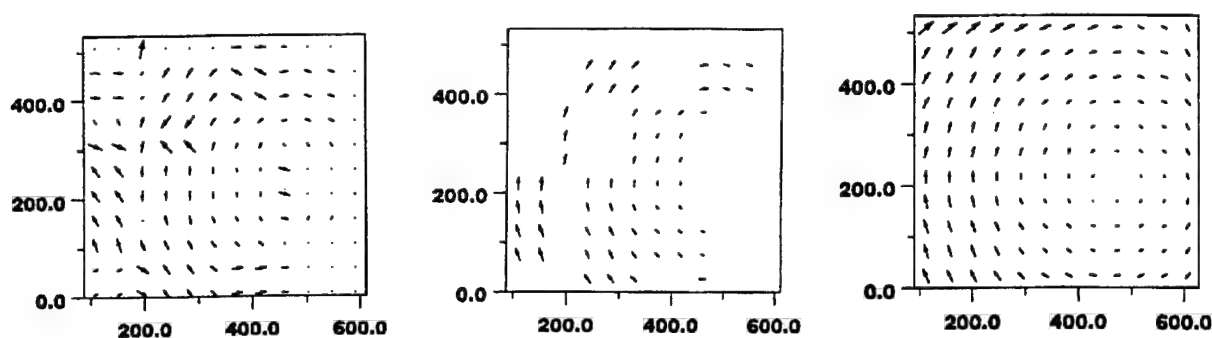


Figure 13b,c,d. Vector Plot of b) Raw Data, c) Data After Bad Vector Removal and d) Data After Interpolation.

## 6. PIV SYSTEM VALIDATION

The overall system was validated through a series of experiments carried out under supersonic, subsonic, reacting and non-reacting flow conditions. The versatility of the system was demonstrated through its implementation under the

different flow conditions. In the following sections, the PIV experiments carried out are reported in detail.

## **6.1 SUPERSONIC EXPERIMENTS**

PIV experiments with the 35-mm camera, the digital CCD camera and the 8 m m video camera were performed in the wall boundary layer region in a Mach 2.9 wind tunnel at the Aerospace Engineering Department of the Air Force Institute of Technology. Experiments were also performed in the same wind tunnel with a wedge placed on the top wall. Turbulent supersonic wall boundary layers occur in many situations of practical interest, such as high speed flight vehicles, supersonic aircraft engine inlets, and flows within high performance compressors. Such flows are analytically difficult to describe and provide a challenging experimental topic. However, the structure of subsonic and supersonic boundary layers has been extensively studied, so that there is a database with which the two color PIV data obtained in this experiment can be compared. The capabilities of the PIV system can thus be demonstrated, and the accuracy of the results tested.

### **6.1.1 WIND TUNNEL TEST FACILITY**

The first series of wind tunnel tests was performed at the Air Force Institute of Technology. A blow down supersonic wind tunnel (Figure 14) provided 25 seconds of Mach 2.8 air flow at the test section. The settling chamber pressure and temperatures were maintained at  $2.0 \pm 0.03$  atm and at  $297 \pm 2$  K. This results in a  $Re/m$  value of  $18 \times 10^6$  in the freestream. Previously recorded data reveal variation in Mach number of  $\pm 0.02$  across the test section, confirming a two-dimensional flow. The cross-sectional area of the test section is constant and measures 6.35x6.35 cm. A pair of Vicor windows mounted in the top and bottom walls of the wind tunnel provide access for the laser sheet light and a quartz window mounted in one sidewall provides a view port for the camera. The other sidewall, which acts as a backdrop for the images, is painted black to reduce spurious light scatter. The coordinate system is defined such that  $x$  is positive in the stream wise direction, with its origin located at

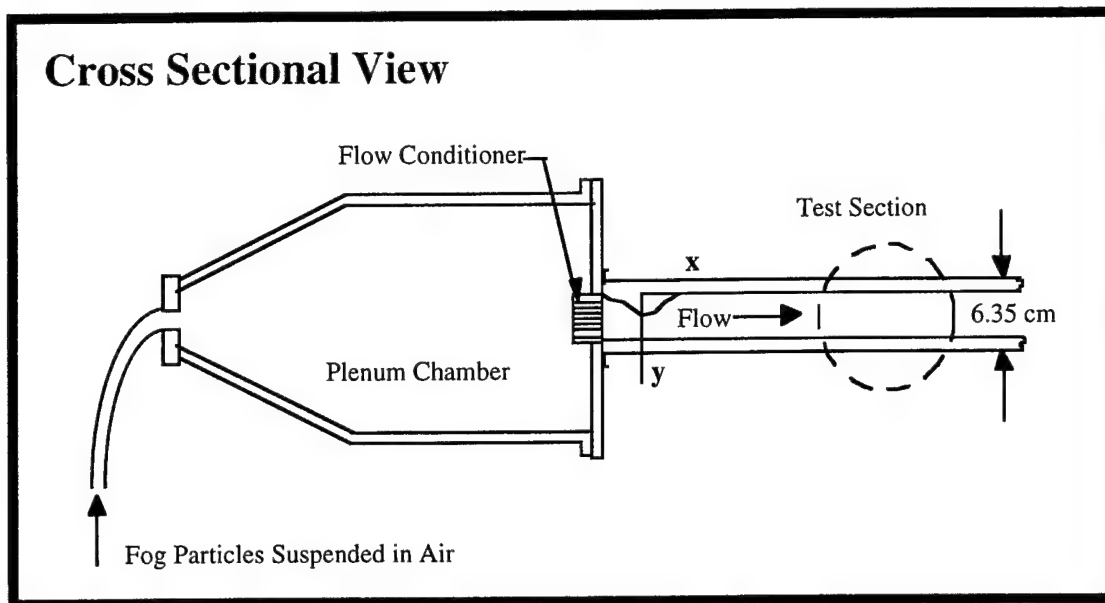


Figure 14. Schematic of Mach 2.9 Flow Facility at AFIT.

the nozzle throat. The streamwise center of the images is located at approximately  $x = 73$  cm. Since the boundary layer of interest is located on the top wall of the wind tunnel,  $y$  is defined normal to the top wall of the test section with its origin at the surface of the wall.  $Z$  is the dimension spanning the wind tunnel. The statistical calculations incorporated data across the image in the streamwise direction as well as from image to image within the image ensemble at each  $y$  location. The boundary layer thickness ( $d = 9.85$  mm) varied by less than  $\pm 0.337\%$  in this region.

### 6.1.2 FLOW SEEDING

A major factor in performing these experiments was the ability to get adequate particle seeding for acquiring the PIV images. The PIV images are captured through Mie scattered light from the seed particles. This meant that the particle sizes used was large enough for Mie scattering and yet small enough to accurately follow the supersonic flow field. Calculations [Adrian 1990] and experiments [Goebel and Dutton 1990] show that particle sizes between  $0.5 \mu\text{m}$  and  $0.8 \mu\text{m}$  were required for the test conditions and light wavelengths used in these experiments. The Mach 2.9 flow is seeded with fog particles (nominally  $0.5 \mu\text{m}$ ) formed from a mixture of

polypropylene glycol and water (fog fluid # 8207 by Rosco) vaporized by a Dantec 2927 UL fog generator. The smoke generator is designed to operate at atmospheric pressure only. In order to get adequate seed particle density in the flow field, the smoke generator was enclosed in a pressurizing chamber which was pressurized to 30 psi. In the present study, smoke is injected into the settling chamber of the wind tunnel through a serrated injection strut mounted just upstream of the flow conditioning. This injection strut was designed to disperse smoke only in the upper half of the tunnel, along the spanwise centerline. This provided sufficient seeding for PIV measurements in the boundary layer on the top wall.

### **6.1.3 DATA ACQUISITION AND ANALYSIS FOR SUPERSONIC EXPERIMENTS**

The PIV images were acquired using a digital CCD color camera and a 35-mm camera. The images were captured on Kodak Gold 400 ASA film. The resolution of the images obtained is dependent on the grain size of the film and the camera magnification. Once the images were captured on film, the film was developed and the negatives digitized using a Polaroid Sprints can scanner. The digitized images were then stored in PICT format for post processing and analysis. A Macintosh Power PC was used to perform all the post processing and analysis. Figure 15 shows a correlation plot in FFT space for a typical image file. In this instance, the image is from a wall boundary layer region of the Mach 2.8 wind tunnel at AFIT. The correlation plot shows the calculated correlation peaks through the arrows shown in the photograph. Figure 16a shows a typical digitized PIV image in the boundary layer region of the flow. The image was captured with a 35-mm camera on Kodak Gold 400 ASA film. The negative was digitized and a 900 x 900 pixel area (Marked with arrows in Figure 16a) was cropped to perform the overall PIV analysis. The flow direction is from right to left. The image shows the red and green scattered light from the seed particles in the flow.

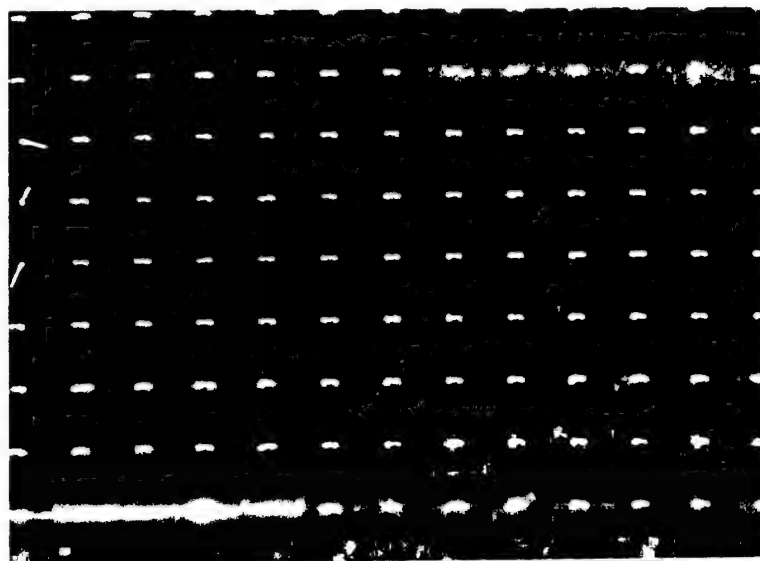


Figure 15. Correlation Plot of a Typical PIV Image in FFT Space.

Once the data analysis was performed, the resulting data was imported into the commercially available Spyglass Transform program to obtain a vector plot. Figure 16b shows a vector plot of the image of the wall boundary layer shown in Figure 16a. The vector plot is shown for the region in the image marked with the white box. In

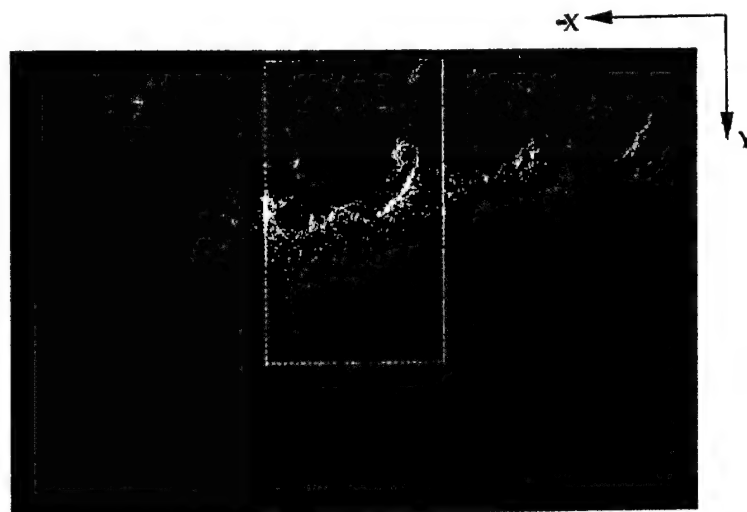


Figure 16a. Digitized PIV Image in the Boundary Layer Region of Mach 2.9 Flow.

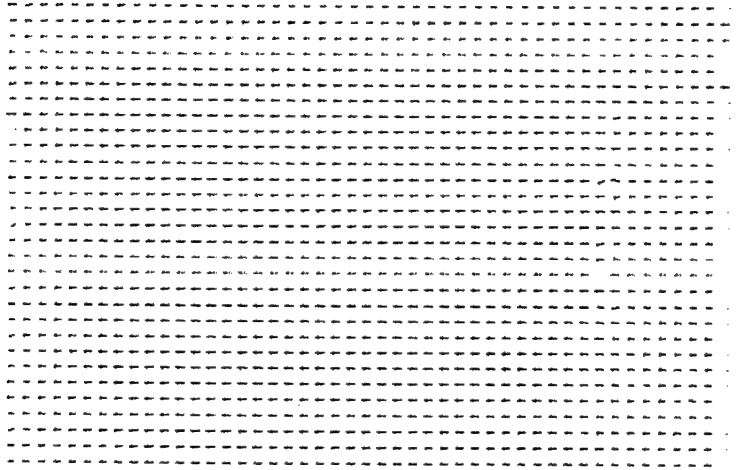


Figure 16b Vector Plot of the Marked Wall Boundary Layer Region.

the vector plot shown, the wall is situated at the bottom of the plot and the top half of the plot is the free stream flow. The length of the arrows is proportional to the displacement vector for the flow. The size of the velocity vectors is also proportional to the flow velocity in the given region. The velocity of the flowfield can be calculated by knowing the resolution of the image and the time delay between the two pulses. The calculated size of the velocity vectors is 16.86 pixels in the free stream and 14.77 in the boundary layer. The measurement resolution was 122.26 pixels/mm. The velocity obtained in the free stream is thus 626.7 m/sec whereas the velocity obtained in the boundary layer is 549.1 m/sec.

Figure 17a is a two color PIV image taken at the Mach 2.8 wind tunnel with a wedge placed at the top wall. This image was captured using a digital color CCD camera system. The white box marks the region of the image that was processed to obtain the velocity vectors. The position of the wedge in the flowfield is also marked in the image with the arrow. The third arrow in the image points to the presence of a weak shock due to the wedge. The data for this image was also processed in the manner described above. Figure 17b shows the vector plot of the 900 x 900 pixel section of the image. The bottom of the plot corresponds to the top wall of the tunnel. The presence of the shock is manifested in the vectors that are directed

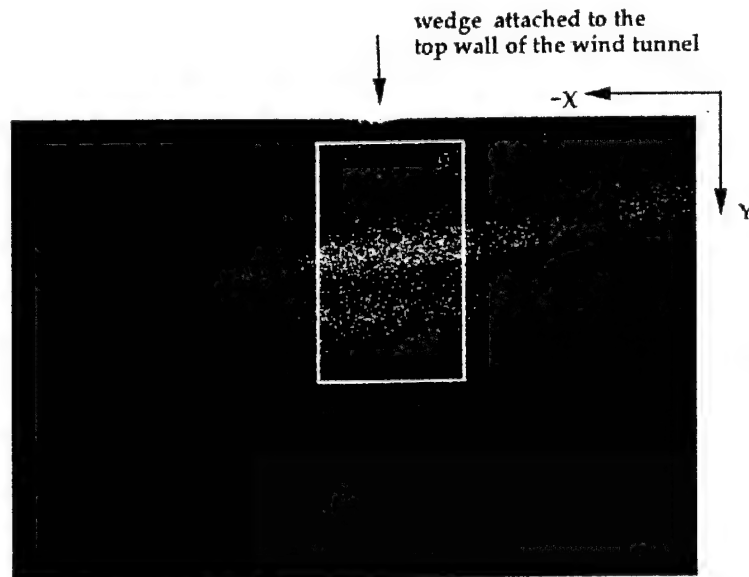


Figure 17a. Two Color PIV Image in Mach 2.9 Flow with a Wedge.

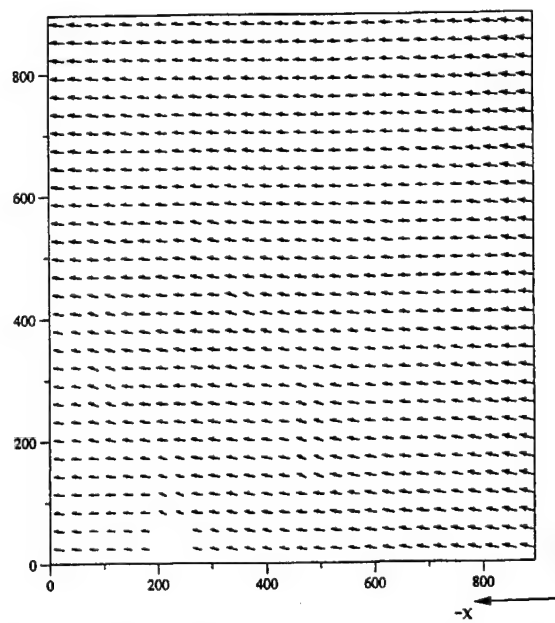


Figure 17b. Vector Plot of the Marked Region of the Wedge Flow.

upward as marked with the arrow. The tilt of the velocity vectors is not very pronounced due to the weak nature of the shock.



## 7. STATISTICAL CALCULATIONS USING PIV MEASUREMENTS

The PIV measurements used for statistical calculations were performed on the same Mach 2.8 flowfield, as described above. The temporal delay between the two lasers set as a function of gas velocity, desired interrogation spot size, and optical magnification ( $m$ ) which is defined as

$$m = \frac{d_{image}}{d_{object}}, \quad (7.1)$$

where  $d_{image}$  is the dimension of the projection of an object onto the image plane (the 3060 x 2036 pixel array in this case) and  $d_{object}$  is the true physical dimension of the object. In the present experiments, two magnifications and, thus, two different time delays were selected and monitored by a photodiode. A 105 mm micro lens with an  $f\#$  of 5.6 was used to record images at a magnification of 0.69. A 2x extension ring was added to obtain a magnification of 1.92. For a magnification of 0.69, a 400-ns time delay was selected, while a 100-ns time delay was chosen for a magnification of 1.92.

### 7.1 DATA ANALYSIS

Once the PIV image was captured and digitized, the velocity field was obtained using the cross-correlation technique. To improve the analysis of the seeded flowfield, the output of the linear camera was convolved with a logarithm-like function prior to cross-correlation analysis. The two-dimensional cross-correlation technique used in the present study is based on intensity maps of the red and green images of scattered light.

The correlation function is calculated over small segments of the PIV image. Thus, prior to processing, the digitized PIV image is dissected into small sub-regions called interrogation spots. The dimensions of each interrogation spot depend on particle seed density, estimated local velocity gradients, particle image size, and desired spatial resolution. The maximum displacement of each particle must be less

than half the interrogation spot size. In the present experiments, the interrogation domain measured  $128 \times 128$  pixels, corresponding to  $1.66 \times 1.66$  mm with 0.69 magnification and  $0.60 \times 0.60$  mm with 1.92 magnification in the measured flow. In order to enhance the overall resolution, the interrogation domains are overlapped by one-half the domain size. The peak of the correlation map corresponds to the average velocity displacement within the interrogation spot.

## **7.2 UNCERTAINTY ANALYSIS**

The experimental uncertainties are calculated based on knowledge of the instrumentation used and a simple root-mean-square error analysis. This method assumes that the contributions to uncertainties arise mainly from unbiased and random sources. Uncertainty in the velocity measurement arises from the time required to keep the large out-of-plane velocity and fluctuating components within the laser sheet during both pulses. The resulting number of pixels of displacement, typically  $> 10$ , and the sub-pixel resolution of 0.1 pixels then dictate an uncertainty of  $< 1\%$ . The data were acquired at resolutions of 1.66 and 0.6 mm, using 77 and 213 pixels/mm, respectively.

### **7.2.1 RESULTS OF UNCERTAINTY ANALYSIS**

In the Mach 2.8 seeded boundary-layer flow, twenty-nine PIV images were recorded with a magnification of 0.69, while five images were acquired with a magnification of 1.92.

Figures 18a and 18b show typical double-pulsed two-color images for  $m = 0.69$  and 1.92, respectively. The field of view for both images is centered at  $\sim x = 73$  cm. The LDV data discussed here were recorded at  $\sim x = 72$  cm. Boundary-layer structures are evident in the top portion of Fig. 18a. The streaks in the middle of the image are due to partial blockage of the holes in the injection strut. The red-green particle pairs are clearly visible in Figure 18b. The typical separation between red and green images in the particle pairs is 13 - 15 pixels in the freestream flow for both

magnifications, based on the time delay and pixel resolution. The red beam was pulsed first. Inspection of the red-green particle pairs in Fig. 18b shows the flow velocity to be from right to left.



Figure 18a. PIV Image of Mach 2.8 Boundary Layer with a Magnification of 0.69.

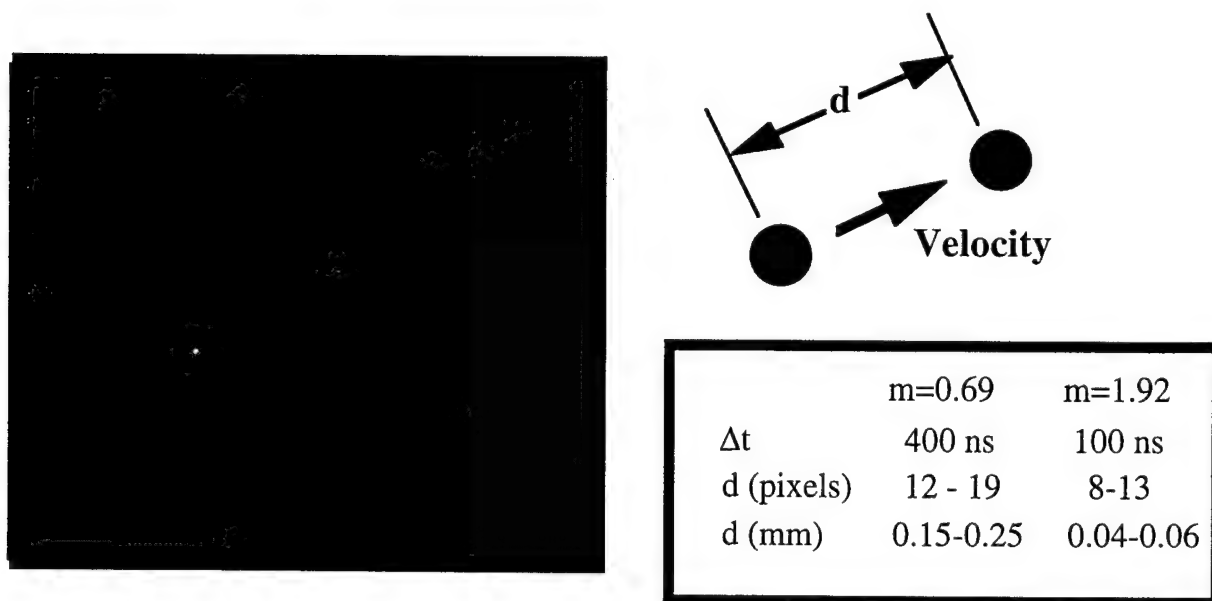


Figure 18b. PIV Image of Mach 2.8 Boundary Layer Flow with a Magnification of 1.92.

Corresponding vector plots are shown in Figs. 19a and 19b. Invalid vectors omitted from the velocity maps account for the blank spots. It is evident that system optimization made it possible to obtain a high percentage of valid vectors. The invalid vectors were due to an insufficient number of particle pairs within the interrogation spots. An increase in the density of seed particles in the flow is required for future experiments to alleviate this problem. Several fog generators are commercially available and warrant investigation for use with PIV, and possibly LDV, systems.

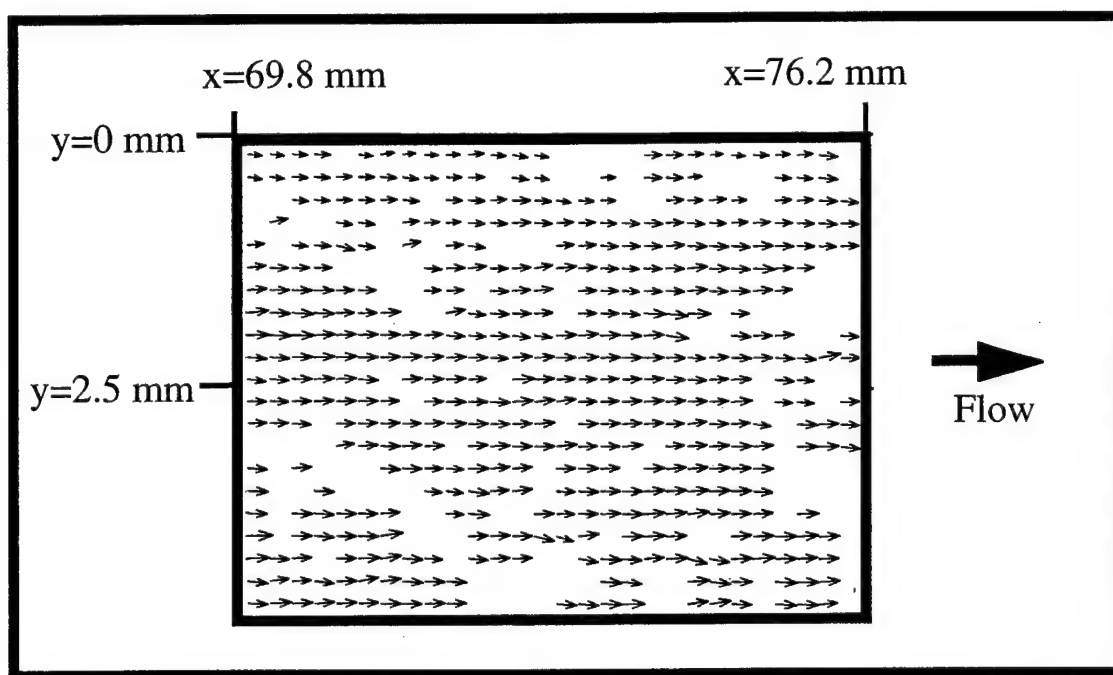


Figure 19a. Vector Plot of Image Shown in Figure 18a.

A consistent transverse velocity  $v \sim 20$  m/s in the freestream flow indicates that the camera was slightly tilted relative to the top wall of the tunnel. This introduces a negligible error ( $< 0.06\%$ ) in the streamwise velocity values. A large tilt would require corrective calculations for both the frame of reference and the measured velocity values.

These experiments were performed with the preliminary time delay circuit which introduced a  $\pm 10$  ns jitter in the time delay which in turn caused the overall velocity measurements to shift a different amount for each image with a maximum deviation of 5%. Normalizing the velocity vectors with the freestream or boundary "edge" velocity for each  $m = 0.69$  image resolved this deviation. A similar normalization for the  $m = 1.92$  images was also performed. Once the valid velocity vectors were determined, the statistical analysis was performed.

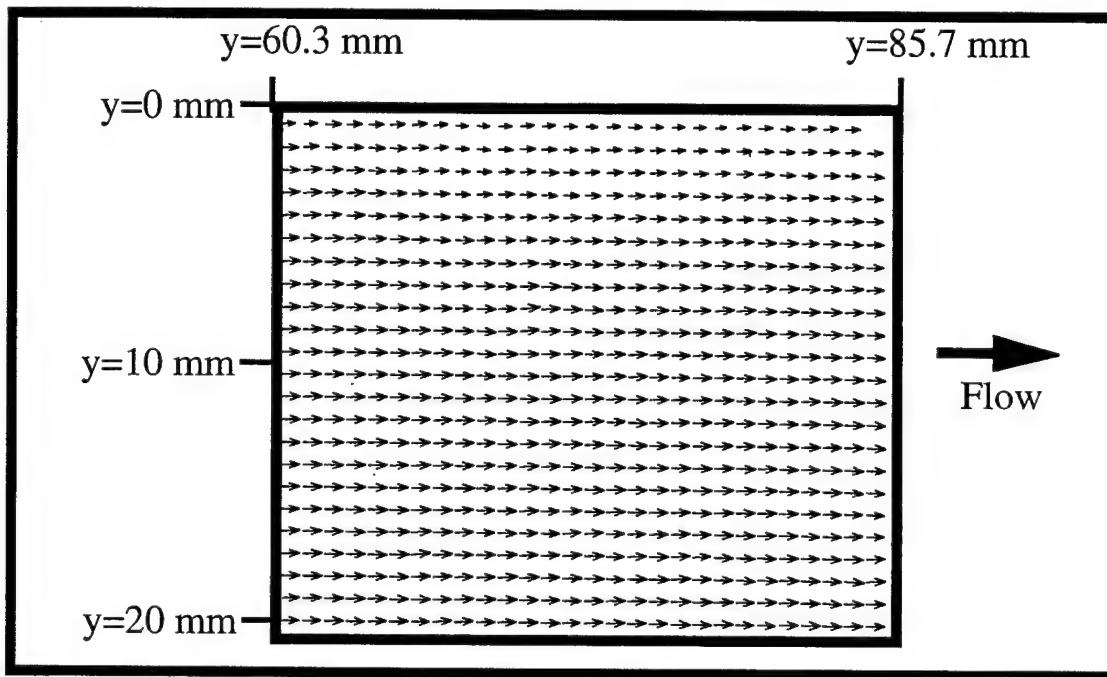


Figure 19b. Vector Plot of Image Shown in Figure 18b.

Mean velocity, turbulence intensity and shear stress values were calculated over the image ensemble for each interrogation spot. Figure 20 shows the normalized mean streamwise velocity values for each interrogation spot as a function of  $y/d$ , where  $y$  is the distance from the wall and  $d$  is the boundary-layer thickness determined to be 9.9 mm in an earlier LDV study. The mean freestream velocity appears to increase as much as 10 m/s across the 18-mm flow region captured in the PIV image (Fig. 21).

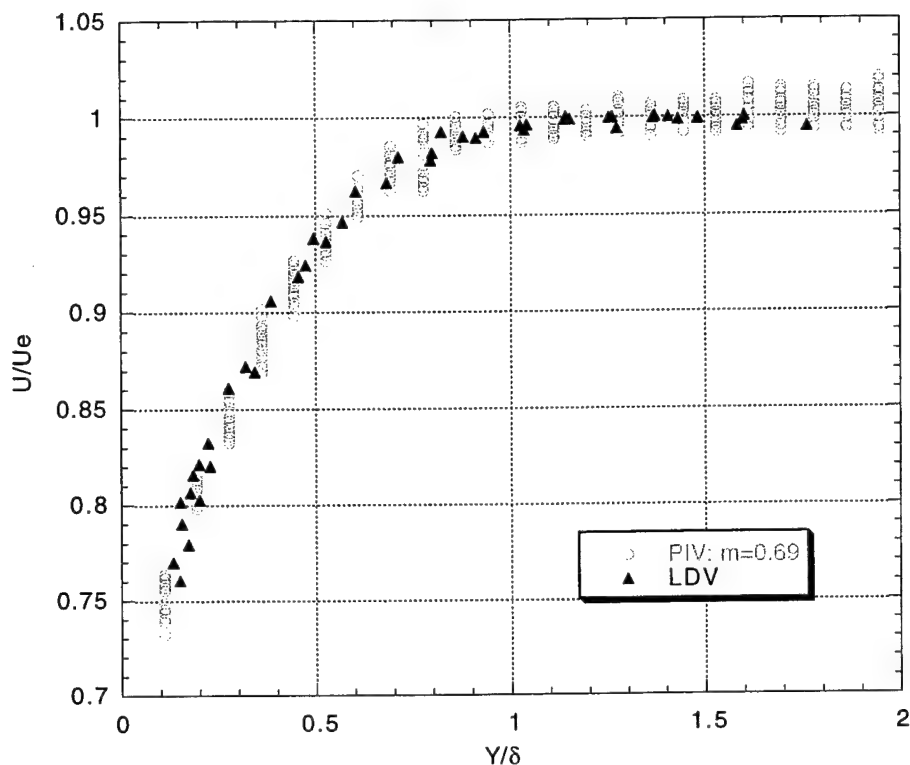


Figure 20. Mean Streamwise Velocity as a Function of  $y/\delta$ .

Figure 22 shows the fluctuation of velocity values for each interrogation spot in terms of normalized RMS values. Again, each data point represents the average value through the 29 images, and the series of points at each  $y/d$  corresponds to the series of interrogation spots across the image in the  $x$ -direction. A portion of the velocity fluctuation is due to the  $\pm 10$  ns jitter in the time delay between laser pulses, as previously discussed. The RMS values for the PIV measurements are equal to the RMS values near the wall and are nearly twice as large as the RMS values for the LDV measurements away from the wall. The size of the sample set used for these calculations greatly influences the RMS values. For PIV, the number of samples remains constant at  $\sim 29$  per interrogation volume, whereas the LDV measurement sample size for each measurement volume varies from  $\sim 5000$  near the wall to  $\sim 30,000$  in the freestream. All other factors being constant, an increase in sample size of this magnitude would cause the RMS values to decrease from the wall to the freestream. The calculated shear stress values are even more sensitive to

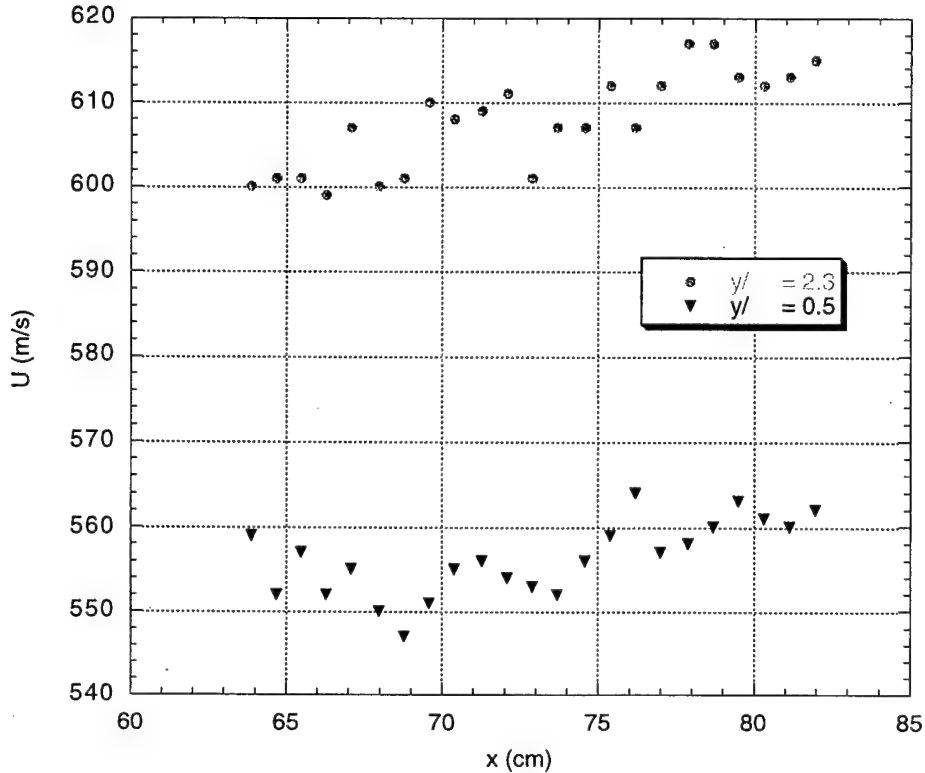


Figure 21. Mean Streamwise Velocity in the Freestream.

the number of samples in a sample set. As expected, the shear stress values calculated from the limited sample of PIV measurements are notably scattered (Fig. 23). In addition to sample size, interrogation volume influences the resulting velocity distribution. The interrogation spot size, similar to the LDV measurement volume, allows for a finite velocity distribution within the interrogation spot itself, which is most significant near the wall where the largest velocity gradients are present. The velocity value at each  $1.66 \times 1.66$  mm interrogation spot is the spatial average for that spot.

Slight deviation in contour shape could be attributed to the compressibility-related velocity biasing which can occur in LDV measurements. If the seed is uniform in the stagnation region of the flow, then as the flow compresses, the regions of highly compressed flow will contain more seed particles than the regions of highly expanded flow. Thus, burst-mode-type LDV processors will "see" more

seed in the compressed regions of the flow. and the results may be biased toward the velocity of the highly compressed region. Generally, this density-bias error is most significant for flows with large density variations (e.g., combusting flows).

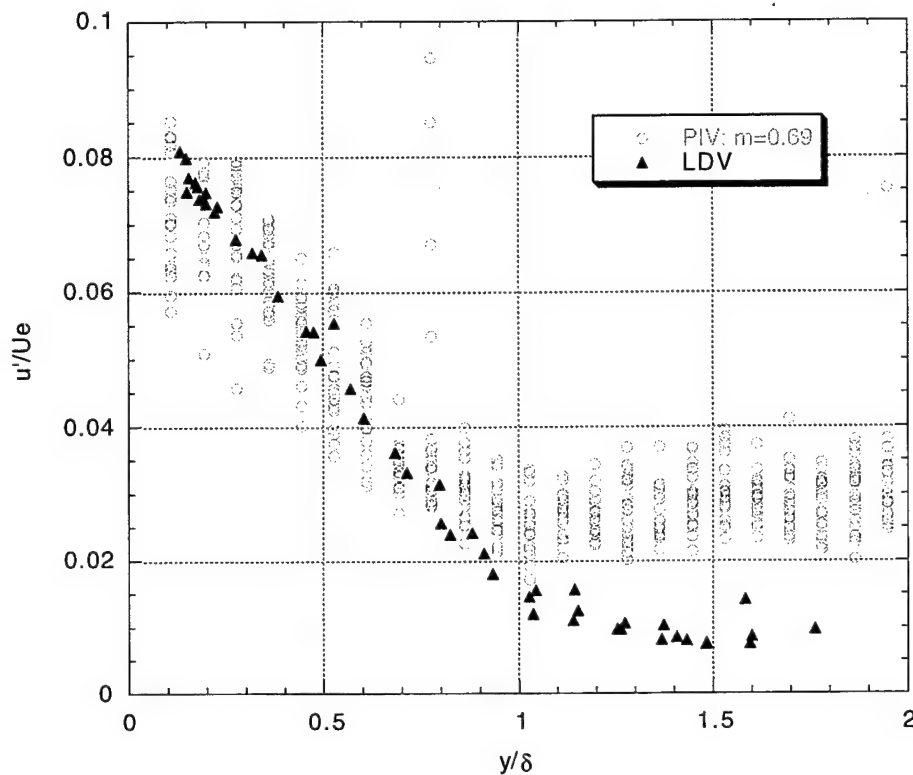


Figure 22. Streamwise turbulence intensity.

In theory, PIV is also susceptible to the density-bias error. However, since the PIV technique does not utilize a Doppler burst, accurate velocity measurements are attainable with minimal compressibility effects. The high spatial resolution and high signal to noise ratio inherent in the digital two color PIV system allow effective measurements of two-dimensional flow velocity in supersonic flows. The PIV results are sufficiently promising to warrant further studies in a well documented supersonic flow with more images per sample set, smaller interrogation size, and increased seeding.



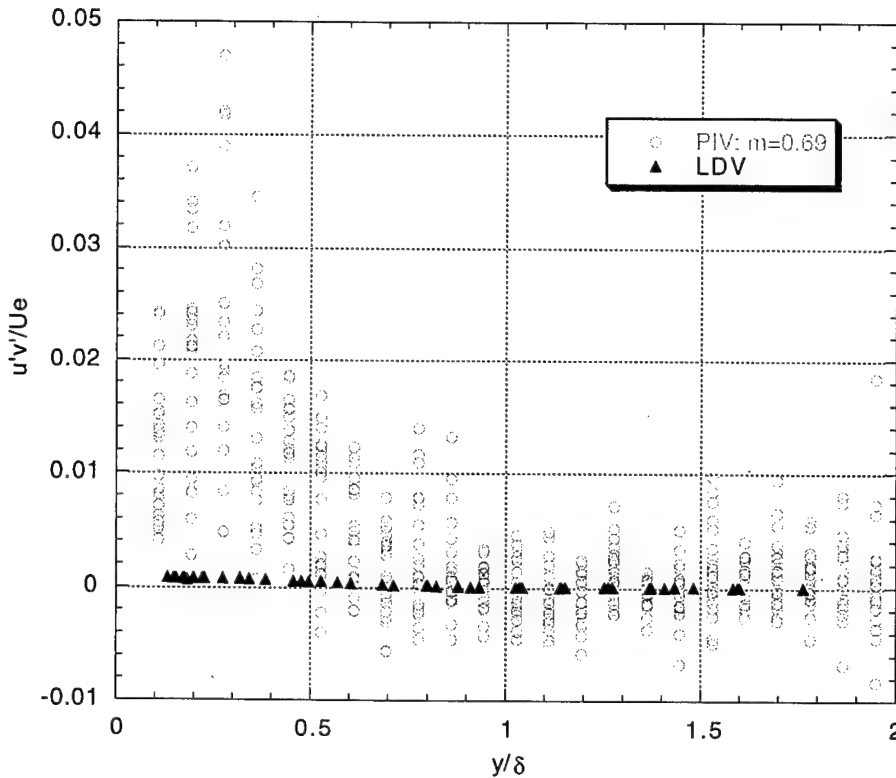


Figure 23. Turbulent shear stress.

The data obtained from the experiments mentioned above were also processed using the software package developed during this Phase II program for comparison. A set of 26 images were used instead of the 29 used in the calculations mentioned above. Figure 24 shows a plot of the average velocity map obtained for the 26 images. The mean freestream velocity obtained is 626.7 m/sec with a velocity of 549 m/sec in the boundary layer region. These results are in good agreement with previously obtained LDV data on the same flowfield. Figure 25 shows a plot of the mean streamwise velocity as a function of  $y$  for a particular  $x$  location. Interrogation volumes of  $128 \times 128$  pixels, corresponding to a spatial extent of  $1.66 \text{ mm} \times 1.66 \text{ mm}$ , were used. The results show the smooth change in the velocity from the freestream to the boundary layer region. Figure 26 shows a plot of the RMS error calculated for the same data shown in Figure 26. The error in the freestream region is shown to be approximately 1.6%, which is similar to the results obtained through LDV.

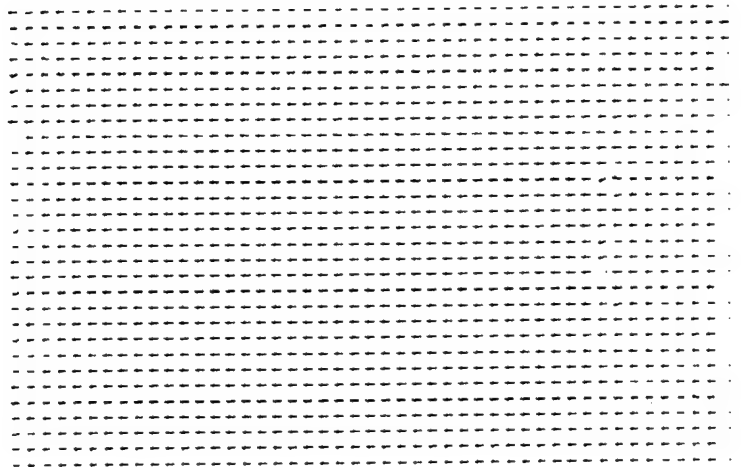


Figure 24. Average Velocity Profile for Mach 2.9 Flow.

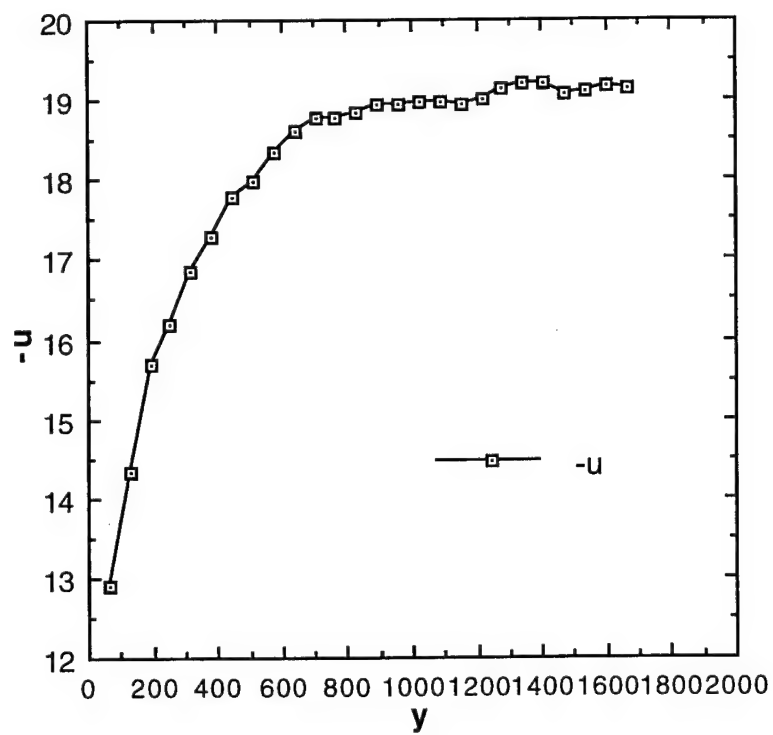


Figure 25. Plot of the mean streamwise velocity calculated with data processed with IMA5 software.

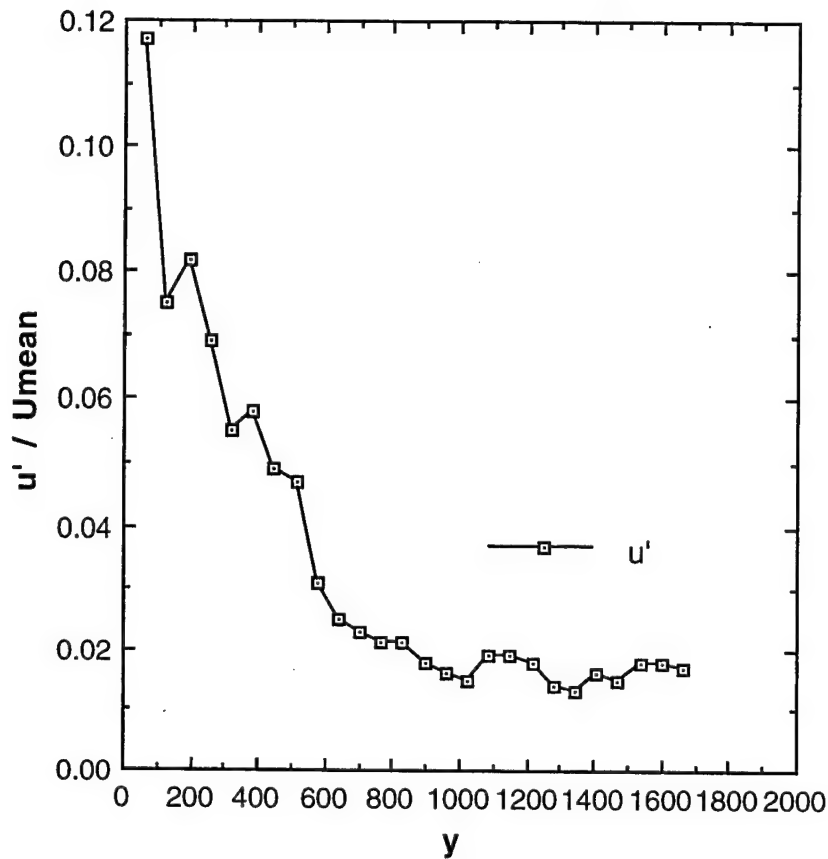


Figure 26. RMS Fluctuations Calculated with IMA5 Software.

The sampling volumes and the data being the same, this data shows the ability of the software package developed through this program to obtain velocity displacement numbers with sub pixel resolution. The software was tested with other sets of data, with similar results as will be discussed later in the report. Figure 27 shows a plot of the turbulent shear stress calculated from the same set of 26 images. The results are shown as a function of  $y/d$ . Data from 2 different  $x$  locations are plotted. The data shows a fair amount of scatter, as expected due to the small sample size. Figure 28 is a plot of the changes in the mean streamwise velocity as a

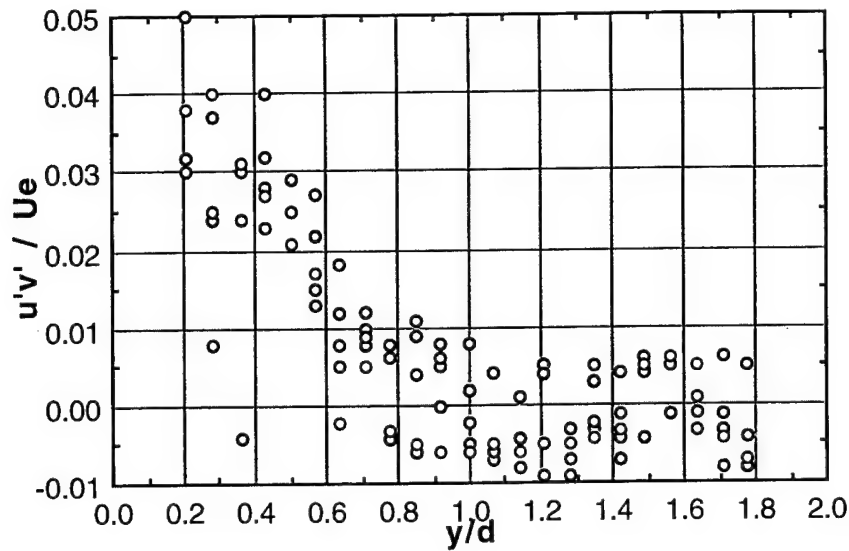


Figure 27. Turbulent Shear Stress Calculated Using IMA5 Software.

function of  $y/d$ . Two different  $x$  locations are plotted here. The triangle data points are from previously acquired LDV data. The data show reasonable agreement. As mentioned previously, typical LDV data use a large number of data samples, typically 3000 -5000 per location in the freestream. The number of samples is reduced by a factor of 2 in the boundary layer region. Considering that the PIV data consists of considerably fewer data samples, the capabilities of the PIV technique are evident.

Experiments were also performed using other boundary layer models in the same blow down wind tunnel facility. Data from those experiments are currently being processed.

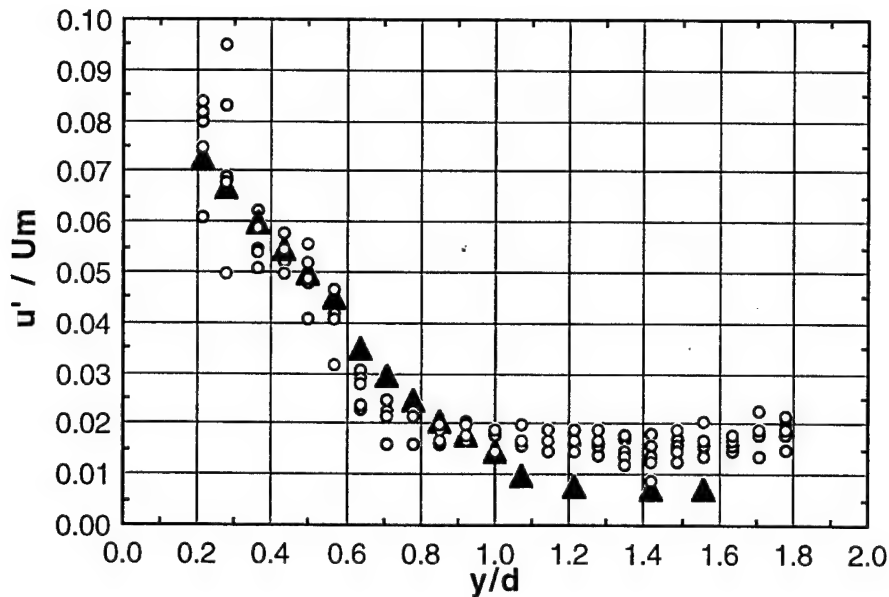


Figure 28. Comparison of Mean Streamwise Velocity Data with LDV Data.

## 8. FLOW BEHIND A BLUFF BODY COMBUSTOR

PIV experiments were also carried out in a subsonic flowfield with a bluff body flameholder. These experiments were performed to test the applicability of the PIV technique in highly turbulent and reacting flowfield. Experiments were carried out under varying resolutions with both the digital camera and the 8 mm video camera. Figure 29 is a schematic of the water cooled combustor and the test section used to perform the PIV experiments. PIV images were taken in the region behind, above and below the bluff body flameholder. The experimental setup for the PIV apparatus was kept the same as in the supersonic experiments. The only change that was made was in the time delay between the red and the green laser pulses. In these experiments, typical delay times in the range of 3  $\mu$ sec to 6  $\mu$ sec were used. The experimental conditions for the flow matched those of earlier planar laser induced fluorescence (PLIF) and LDV experiments. Experiments were carried out with

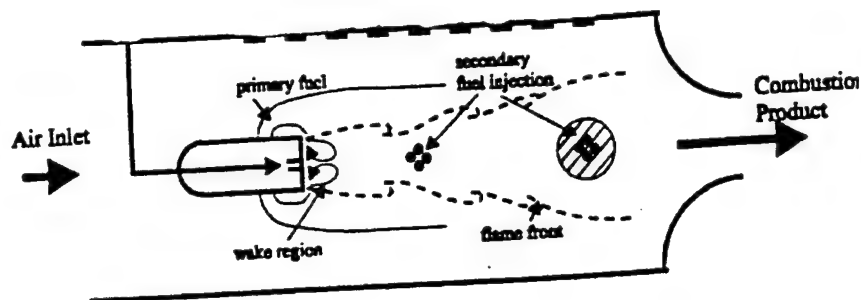


Figure 29. Schematic of the Water Cooled Combustor Test Section.

different image magnifications and resolutions in order to capture different features of a highly turbulent flow regime.

The flow seeding was performed using the Dantec smoke generator which was placed in a pressurized vessel in order to match the pressure in the flowfield. The seed particles were inserted in the settling chamber upstream of the screens in the tunnel. This arrangement provided the most uniform seed distribution. The smoke particles were used both in the nonreacting and the reacting experiments. In addition to the smoke generator, solid aluminum oxide particles were also used to seed the fuel jet in the reacting case. The solid particles were estimated to be  $3\text{ }\mu\text{m}$  in diameter. In the following, a description of the experiments performed and the results obtained is presented.

### 8.1 DATA ACQUISITION

Initial experiments were carried out under non-reacting flow conditions with varying image resolutions. The first set of experiments were performed with the sheet width around 1.5 inches in the test section. Four different locations were imaged with some overlap in order to capture the whole flow field near the bluff body. Figure 30 a,b,c, and d show the digitized images of the four locations imaged. The location of the bluff body is marked on the right hand side of the images. These images were enhanced for display purposes although the image processing is performed on the raw image files. The time separation between the red and the

green laser beam was 3  $\mu$ sec for the displayed set of images. The image resolution was measured by imaging a grid with the camera at the test location. The digitized image grid was then displayed and the resolution measured using the marks on the grid and the pixel area covered on the camera. For the set of images shown in Figure 30, the resolution was 79 pixels/mm. This resolution was achieved by using a 105 mm micro-lens with an f-number f 5.6 and two expansion rings. The images were taken by setting the camera to an exposure time of 125 msec. This ensured that both the laser pulses would be captured in a single

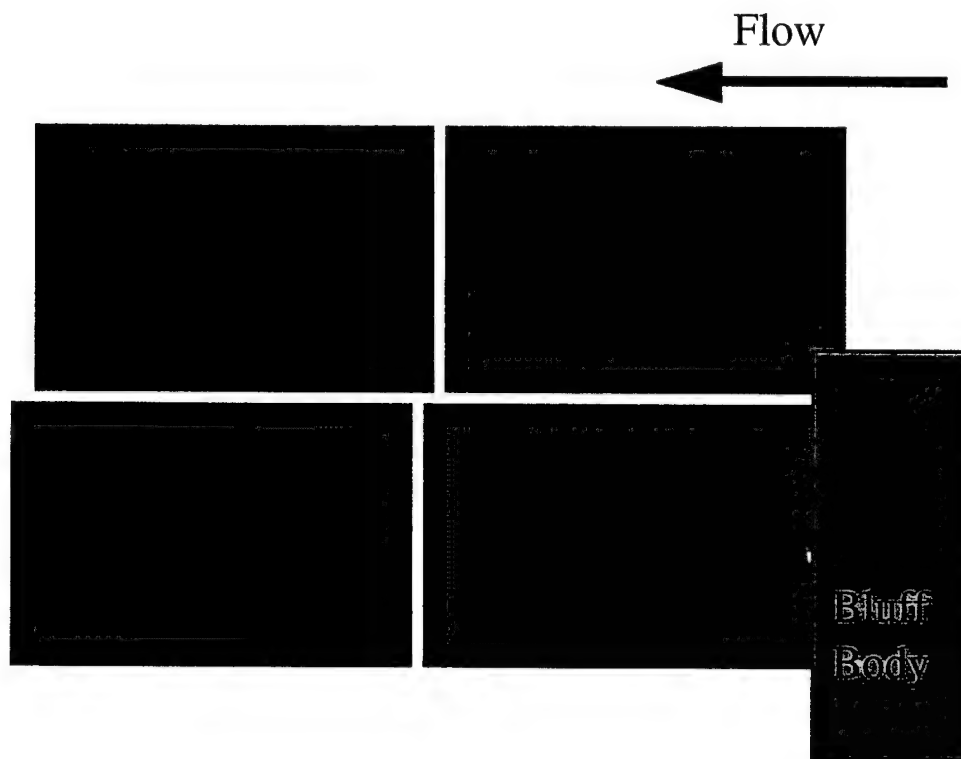


Figure 30a,b,c,d. Two Color PIV Images of Flow Behind a Bluff Body.

image frame. Since the facility has a continuous flow, a number of images were taken at each location under the same experimental conditions so that statistical analysis of the data obtained could be performed. For the conditions shown in Figure 30, 45 images were taken for each location.

Data was also gathered for other test conditions. Figure 31 is a typical digitized image for the flow behind the bluff body. The image was enhanced for display purposes. In this case, the optical sheet size was increased to 2.5 inches and the magnification of the camera reduced to capture the whole flowfield in one snapshot. The location and size of the bluff body is marked on the right hand side of the image. The laser sheet was located at the center of the bluff body and the location of the fuel injector was illuminated by the laser sheet. The resolution of the image was determined using the grid to be 60 pixels/mm. The overall size of the image area is 2.5" x 2". 35 images were acquired under these conditions. The flow conditions were similar to those described in the previous set of images. The sheet thickness is estimated to be 0.9 mm.

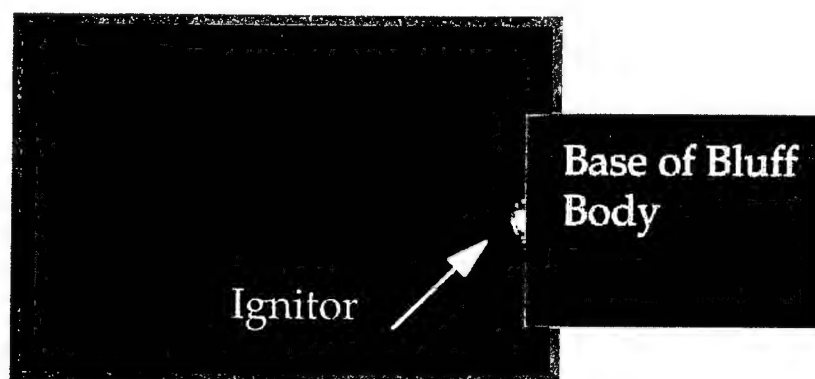


Figure 31. Two Color PIV Image for Flow Behind a Bluff Body (Expanded Image Area).

Experiments were also performed with the bluff body removed from the flow path in order to determine the freestream conditions for the tunnel for comparison purposes. Figure 32 is a sample image of the freestream flow in the test section. The seeding was performed as described above. 38 images were taken in this configuration. The time separation between the red and green laser beams was set at 6  $\mu$ sec and the image resolution was 52 pixels/mm. The location of the image was the same as for those images with the bluff body. The set of 38 images was then used



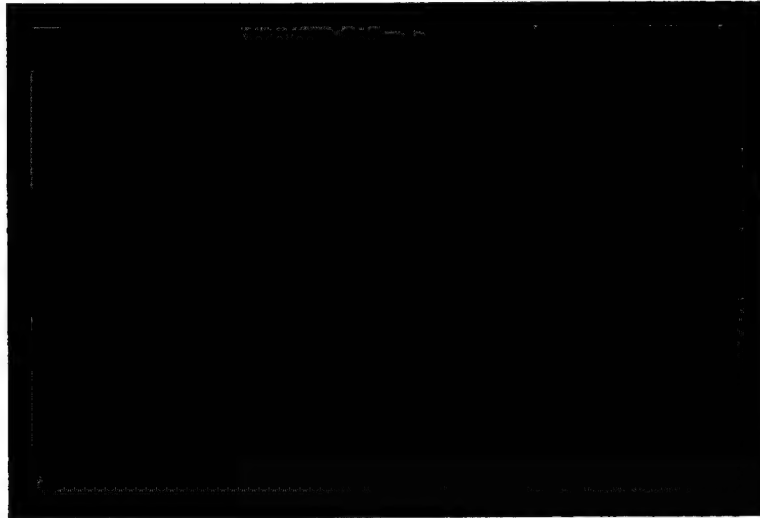


Figure 32. Two Color PIV Image with No Bluff Body.

to compute a mean streamwise velocity field and to obtain the RMS fluctuation in the measured data.

## **8.2 NON-REACTING FLOW BEHIND A BLUFF BODY - PIV DATA ANALYSIS**

The PIV data obtained were analyzed using the IMA5 software developed by Taitech, Inc. during this Phase II program. Figure 33a is a vector plot of an image of the flow behind a bluff body (image shown in Figure 30c). The analysis was performed with a  $128 \times 128$  pixel area interrogation region. Since the image flow is largely behind the bluff body, the flow pattern is highly turbulent and unsteady. The plot shown is a simply processed file without any "bad vector" removal procedure or subsequent interpolation performed. This shows that the seeding in the test region was uniform and provided enough particles for data processing. Figure 33b shows a vector plot of the same data file processed using a  $64 \times 64$  pixel interrogation region. The processing still yields close to 100% good vectors in the central region of the laser sheet indicating excellent seed density and concentration. The extreme right hand region has very few seed particles since it is located just behind the bluff body. Figure 33c shows the same image analyzed using a  $32 \times 32$  interrogation area.

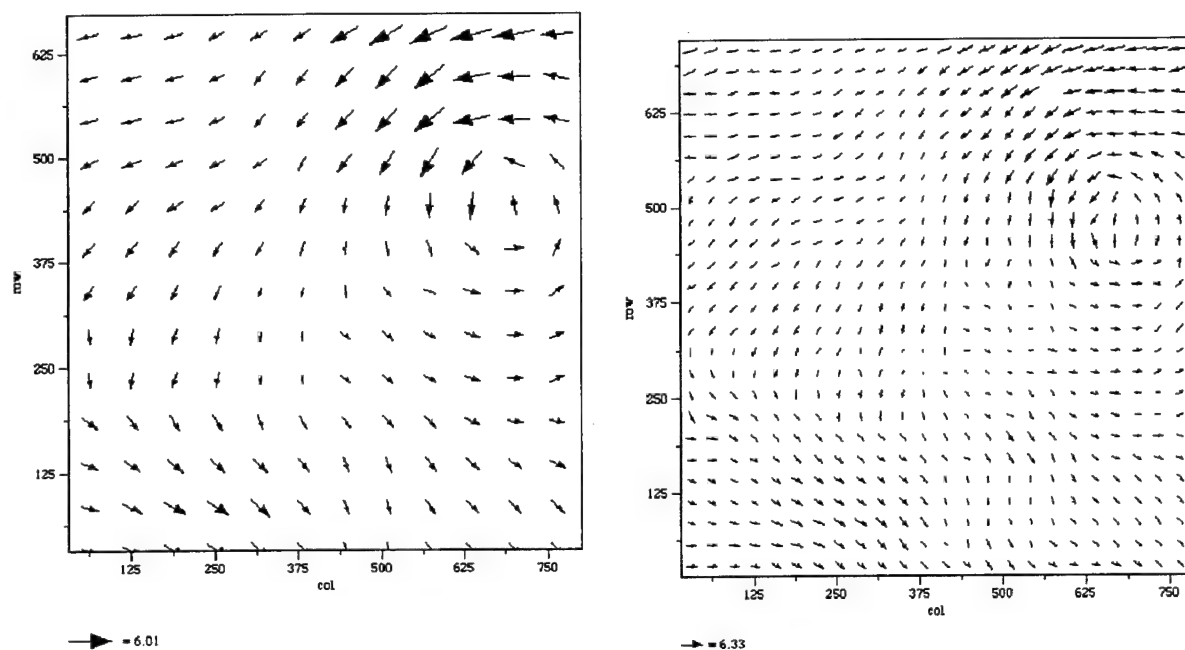


Figure 31a,b. Vector Plot of Image in Figure 27c. Analysis Performed by Using a) 128 x 128, and b) 64 x 64 Interrogation Region.

The success rate is about 80% indicating that the spatial resolution selected and the seed density used are close to the experimental limits for the given arrangement. Overall, this set of data demonstrates that the PIV imaging process is perfectly tuned to the test region and the resulting data quality is excellent.

Figure 34 is a plot of the instantaneous 2D velocity map of the PIV image shown in Figure 31. The position of the bluff body is marked on the right end of the plot. The highly unsteady and turbulent nature of the flow is clearly evident in this image. A 64 x 64 pixel interrogation area was used to identify this velocity field. The region next to the bluff body does not process as well as the rest of the image due to the lack of seed particles. Figure 35 shows a streamline plot of the same area. Several instantaneous images were taken at this location, all of which demonstrate the highly unsteady nature of the flow. In this particular image, the interrogation

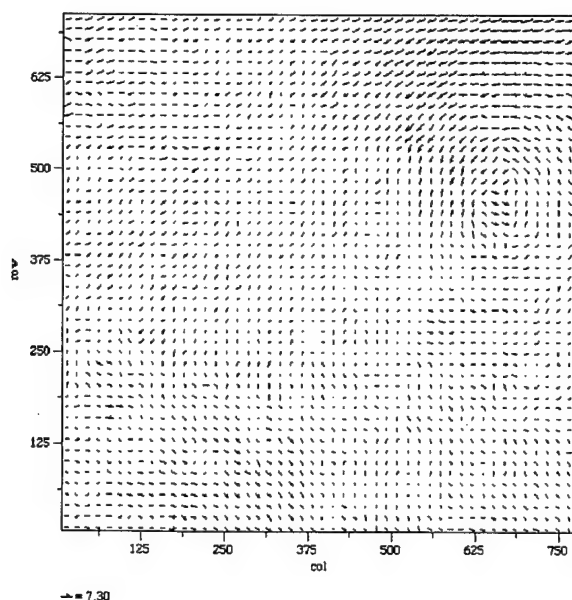


Figure 31c. Vector Plot of Image in Figure 27c Analyzed Using a 32 x 32 Interrogation Region.

region is considerably larger than that shown in the previous set of images. The area shown in the image is 2.5 inches x 2 inches. Once again, the strikingly high

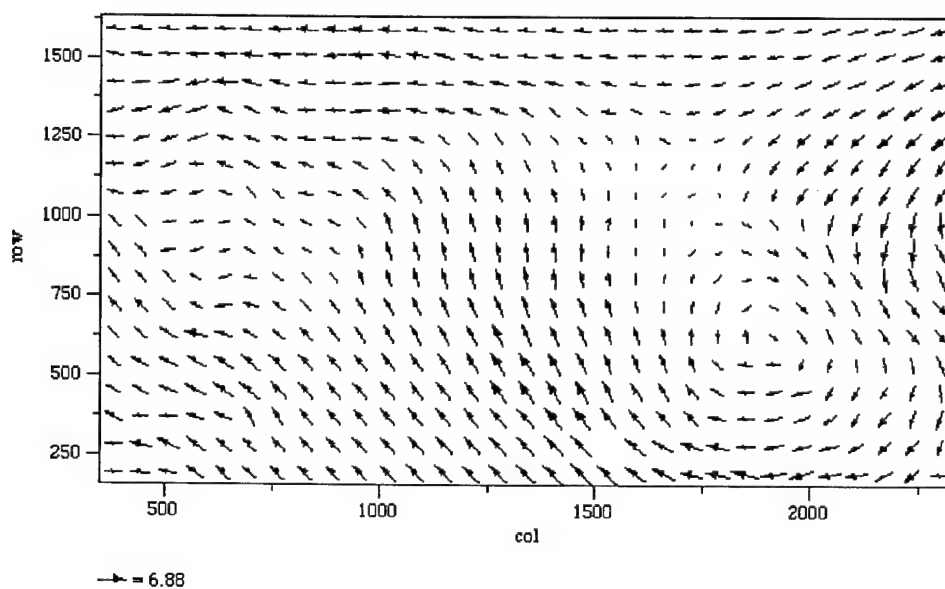


Figure 34. Instantaneous Velocity Map of Image Shown in Figure 31.

number of "good vectors" in the raw data file shows the uniformity of the seed particles and the clarity of the imaging process in the highly turbulent region behind the bluff body.

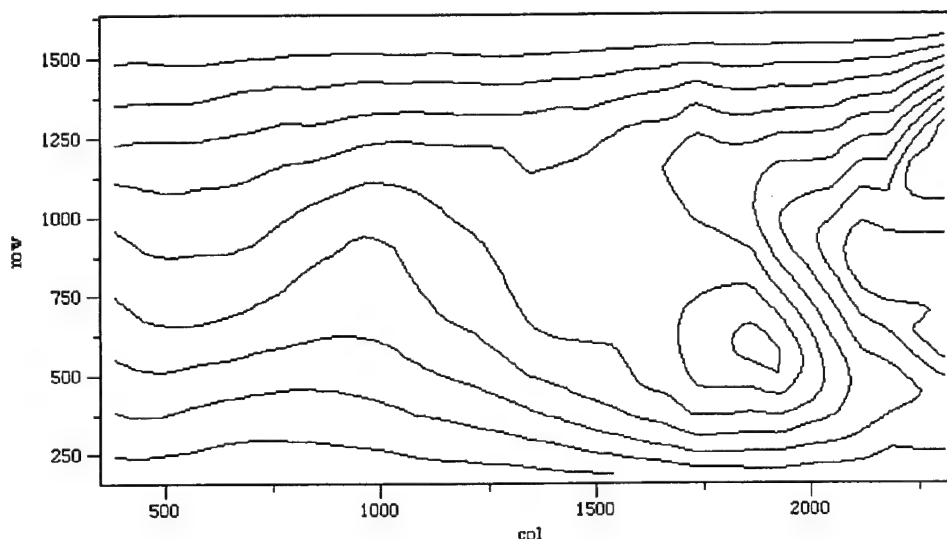


Figure 35. Streamline Plot of the Data Shown in Figure 34.

Figure 36 is a 2D vector plot of the same area of the test section shown in Figure 32 but with the bluff body removed from the flowpath. The plot shows that the flow in the test region is indeed laminar in nature. The calculated streamwise velocity was 77 ft/sec. So far, only instantaneous images were processed and displayed. Since groups of images were taken for each flow condition and image definition, statistical parameters for the flowfield were also calculated using the obtained image groups. A description of the statistical calculations performed and the data obtained is presented below.

### **8.3 STATISTICAL CALCULATIONS OF FLOW PARAMETERS**

In order to perform the statistical calculations with a group of instantaneous PIV images, the IMA5 image processing program was run in a batch mode (described above). One of the images from the group was used to determine the correct set of run parameters and then the whole set of images were automatically processed and

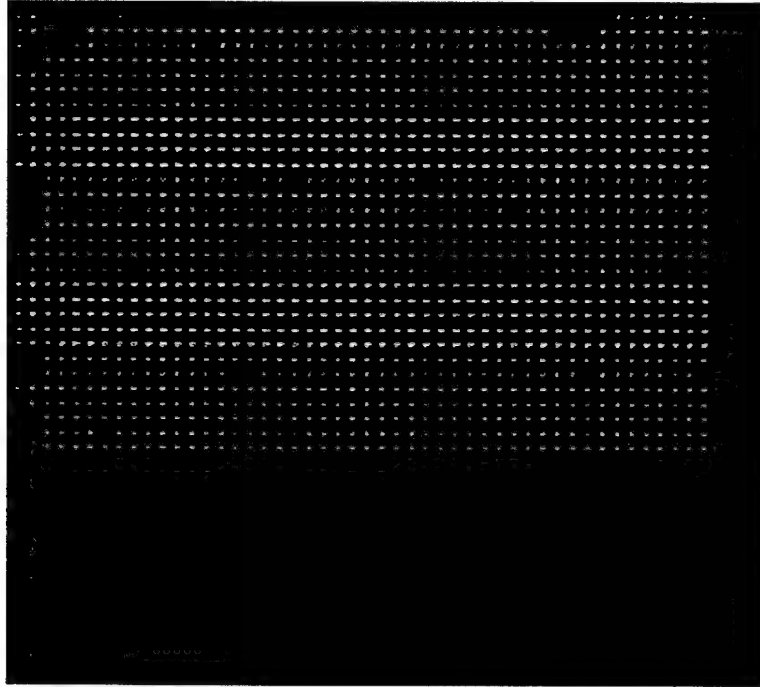


Figure 36. Averaged Vector Plot of Flow (No Bluff Body).

the output from the programs written to individual data files. Once all the instantaneous images were processed, the data files from all of the images were used to calculate a mean velocity field. Once the mean velocity field was created, statistical operations such as RMS fluctuations, turbulence intensity and shear stress values were also calculated. Figure 37 shows a mean 2D velocity map calculated using the group of 35 images calculated for the flow behind the bluff body as shown in Figure 32. The flow in the image is from right to left. The mean velocity map shows several key features of the velocity field, the freestream flow in the regions above and below the bluff body, and the recirculation region in the region behind the bluff body. A streamline plot of the same mean velocity distribution is shown in Figure 38. The streamline plot was calculated using the centerline as the reference. The RMS errors were then calculated about this mean velocity field. Once again, the streamwise velocity was calculated to be 77 ft/sec which is in close agreement with other measurements performed on the flowfield and the calculated value of the velocity. Figure 39 is a plot of the shear layer stresses behind the bluff body obtained from the PIV data. The stresses are plotted as a function of  $y$ . The

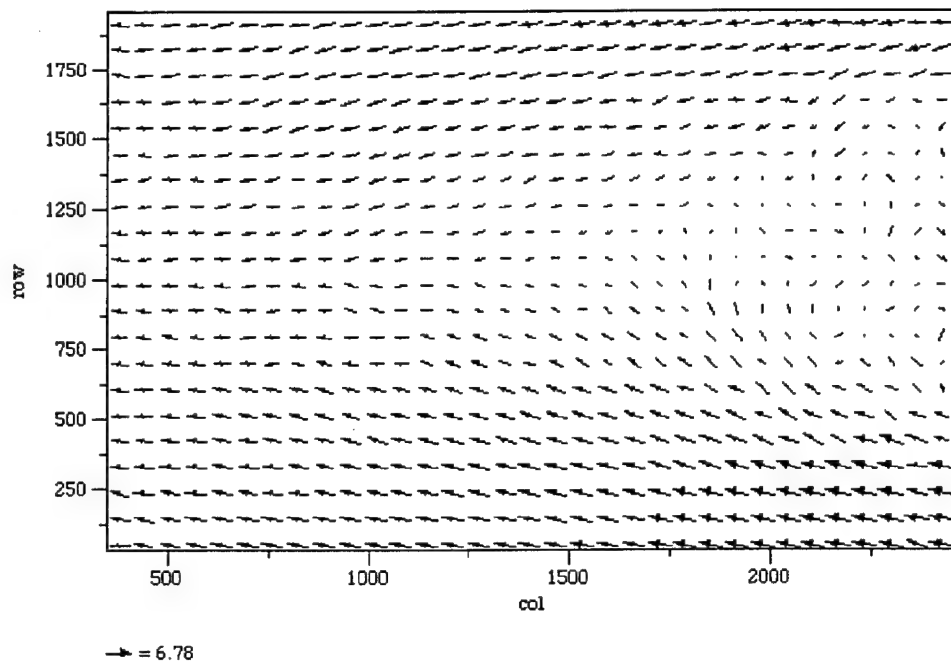


Figure 37. Averaged 2D Velocity Map for Flow Behind Bluff Body.

stresses are close to zero near the  $y = 0$  location, which is closest to the freestream region of the flowpath. As  $y$  the pixel number increases, the region

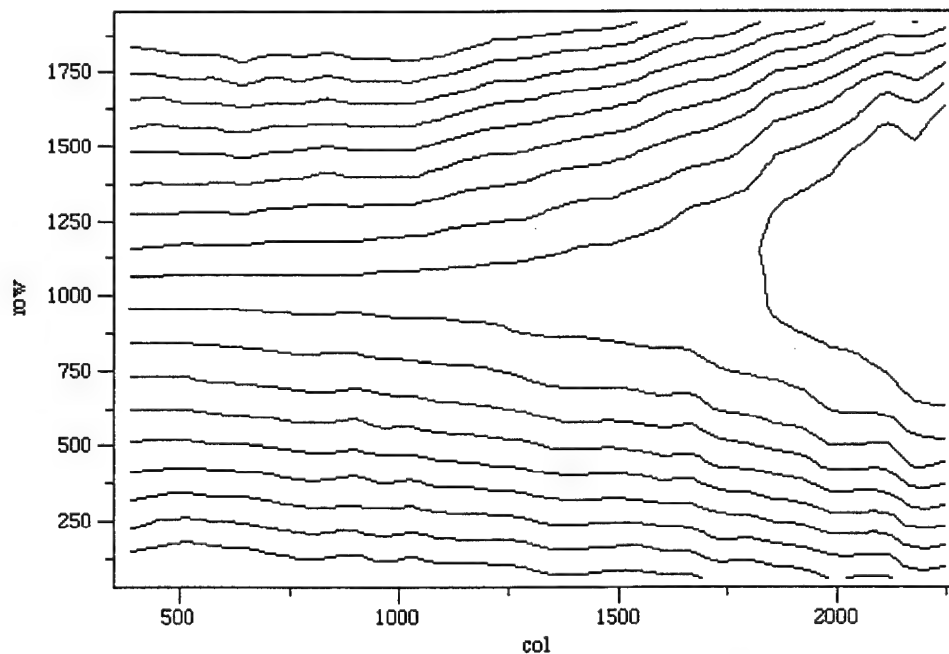


Figure 38. Streamline Plot of the Averaged Velocity Field Shown in Figure 35.

under investigation approaches the region behind the bluff body, which explains the increase in the shear stress.

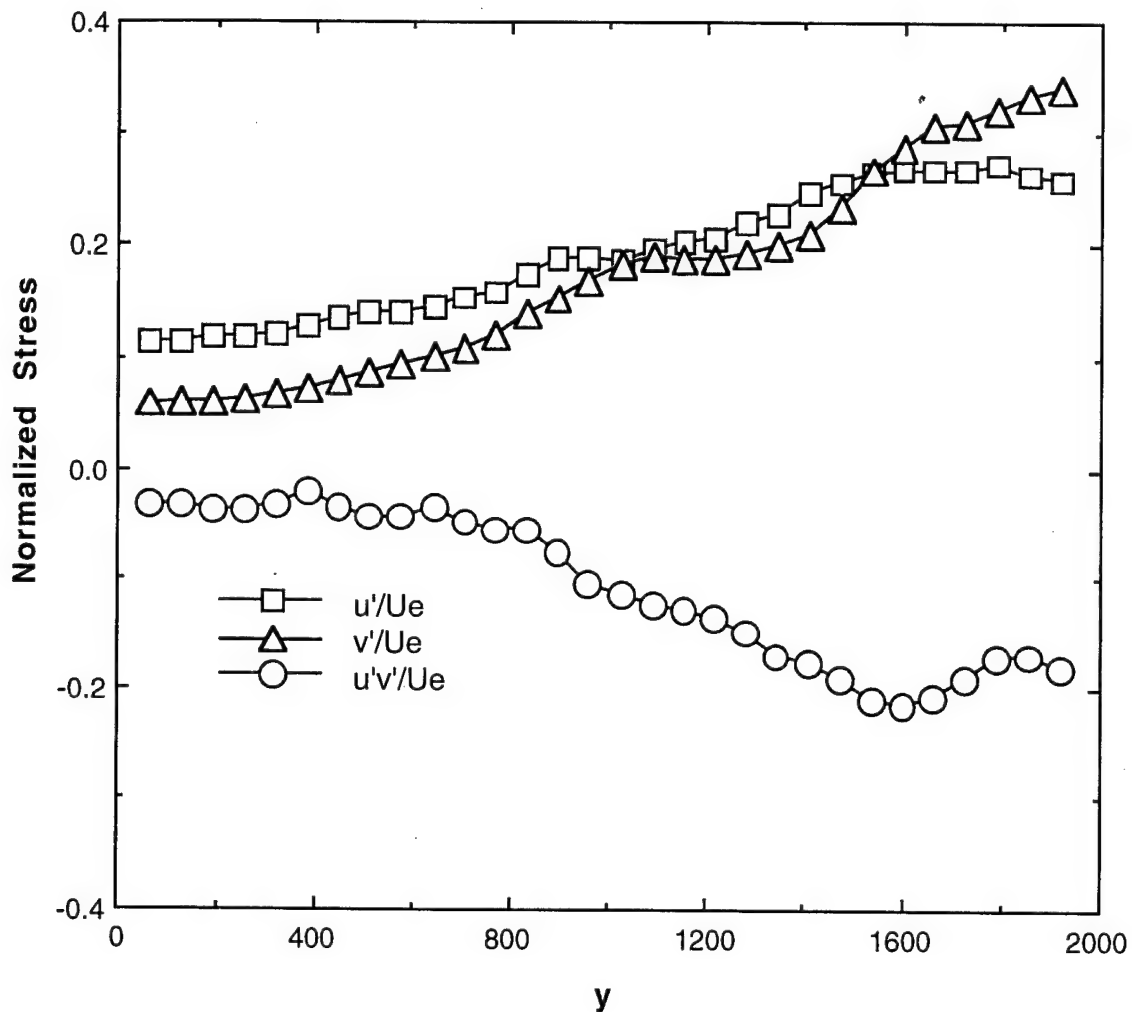


Figure 39. Shear Layer Stresses Behind a Bluff Body.

Figure 40 shows a plot of  $u$  and  $v$  components of the velocity. The rms fluctuations are found to be in the 6% to 7% range. Since the same software and PIV imaging process was used to analyze the supersonic data discussed earlier, this excess fluctuation is attributed to the flowfield itself. This hypothesis was confirmed with preliminary LDV experiments.

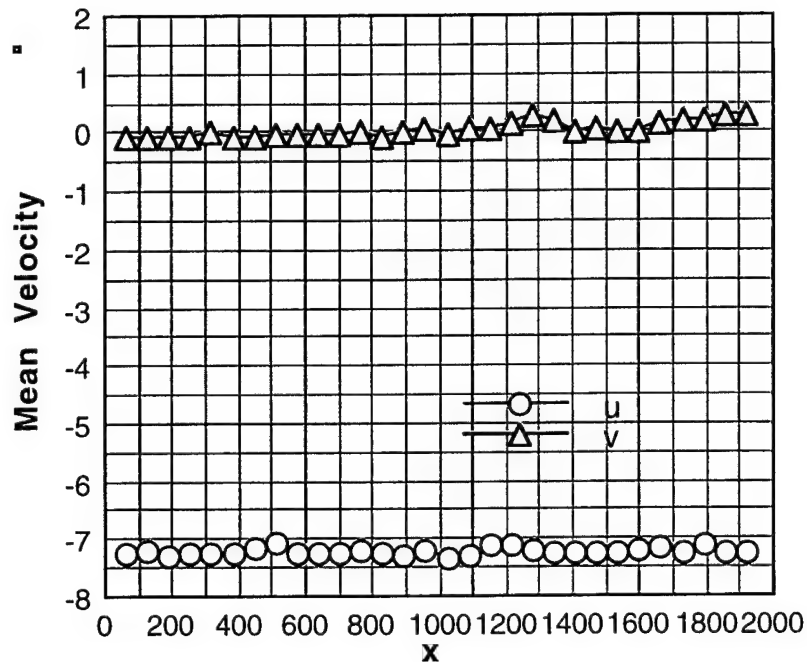


Figure 40. Plot of u and v Components of Velocity Obtained from PIV Analysis for Flow without Bluff Body.

#### 8.4 BOUNDARY LAYER EXPERIMENTS

PIV experiments were also carried out in the boundary layer region of the flow in the water cooled combustor rig. These experiments were carried out with the bluff body flame holder removed from the flow path. The results obtained through these measurements are being processed. The results obtained will be reported in an addendum to this report.

### 9. REACTING FLOW EXPERIMENTS

Following the experiments in the non-reacting flowfield, experiments under combustion conditions were also carried out in the same facility. Propane gas was injected at 1.5 lbm/sec into the air stream. Two 516" injectors are flush mounted on



the top and bottom surfaces of a bluff body which is 1" thick. The flame has been found using high speed videography to exhibit a low frequency large amplitude oscillation. Based on 1-D LDV measurements, the vortex shedding frequency under non-reacting conditions about 230 Hz. Under reacting conditions, combustion instabilities were observed at a much lower frequency of 53 Hz. This frequency agrees with the flame front flapping frequency observed from videography and yields a Strouhal number of 0.07.

Instantaneous PIV measurements were performed to determine the velocity characteristics of the reacting flow. A majority of these images are currently being processed, but a sampling of the data obtained is presented here. Figure 41 shows a

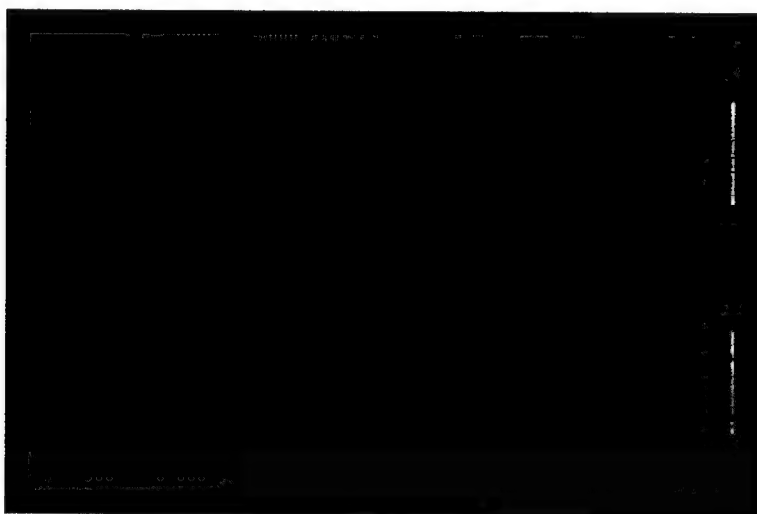


Figure 41. Two Color PIV Image of Reacting Flow Behind the Bluff Body.

PIV image of the flame in the water cooled combustor rig. The image was taken using the Kodak digital camera with an exposure time of 125 msec. The PIV interrogation sheet was placed at the center of the injector region. The freestream as well as the fuel input jet were seeded. The freestream was seeded with the smoke particles and the fuel jet was seeded with alumina particles described above. As can be seen from the image, the blue light from the flame emission itself is extremely dominant due to the large exposure time used. Despite the presence of a large

amount of flame emission, the PIV image processing software yielded a vector field which contained 75% good vectors. The region behind the recirculation zone is more noisy because of the lack of seed particles in that region. The velocity field does not show much change from the non-reacting case because at the center of the injection region, there is no flame present. This was confirmed by LDV and PLIF measurements performed earlier in the same test rig under the same experimental conditions. In order to reduce the presence of the flame emissions from the images, experiments were performed by using a gated camera exposure. This technique will be explained in detail in an addendum to this report.

## 10. CONCLUSIONS

A two color particle imaging velocimetry system was demonstrated for obtaining two dimensional velocity measurements in a subsonic reacting flow and in a supersonic flowfield. The overall system was designed and integrated for use in subsonic or supersonic flowfields. Data was obtained using three different camera systems, an 8-mm video camera, a digital color CCD camera system and a 35-mm camera. The data obtained from the wall boundary layer region in the supersonic wind tunnel showed good correlation with LDV data on the supersonic wall boundary layer studied. The versatility of the system was demonstrated through these experiments. Experiments were also performed in a subsonic flowfield with a bluff body flameholder. The flow in the wake region of the flameholder was investigated using the PIV system developed through this Phase II contract. The results obtained through these experiments showed that the PIV system was capable of resolving the flow information in the highly turbulent region with high degree of accuracy. Values of shear layer stresses behind the bluff body region were also calculated from the PIV data. Experiments were also performed in the boundary layer region of this flow. The data from these experiments is currently being processed and will be reported in an addendum to this report.

Experiments were also carried out in a reacting flow in the same flowfield with the bluff body. These experiments once again showed the ability of the PIV system to resolve velocity fields in a highly turbulent, large gradient flow regime. Different seeding techniques were also experimented with through these reacting flow experiments. In addition, the software used to analyze the PIV data, which was developed independently through this contract, yielded RMS fluctuations in the 1.5% range which is less than the 2% limit widely reported in the literature. The software was developed for the Macintosh platform on which it was primarily used in this work, but can be readily converted to other platforms such as the IBM PC or the UNIX workstation environments.

Presently, in addition to processing the data taken with the system, avenues for commercializing this PIV system are being investigated. The system is currently being advertised on the World Wide Web on Taitech, Inc.'s home page (<http://www.erinet.com/taitech>). Interest has been shown by several groups of researchers. Taitech, Inc. is currently in the process of assembling a Digital Two color PIV system for Yale University. Delivery and setup are expected to be completed in the next 6-8 weeks.

## 11. REFERENCES

Glawe, D.D., Samimy, M., Nejad, A.S., and Chen, T.H., "Effects of Nozzle Geometry on Parallel Injection from Base of an Extended Strut into a Supersonic Flow," AIAA Paper 95-0522, January 1995.

Gruber, M.R., Nejad, A.S., Chen, T.H., and Dutton, J.C., "Large-Scale Convection Velocity Measurements in Compressible Transverse Injection Flowfields," submitted to the 34th AIAA Aerospace Sciences Meeting, Jan. 1996.

Lempert W.R., Zhang, B., and Miles, R.B., "Stimulated Raman Scattering and Coherent Anti-Stokes Raman Spectroscopy in High Pressure Oxygen," *J. Opt. Soc. Am. B*, Vol. 7, No. 5, p. 715, May 1990.

Tennekes, H. and Lumley, J.L., A First Course in Turbulence. Cambridge, MA: MIT Press, 1972, 248-256.

Goss, L.P., Post, M.E., Trump, D.D., and Sarka, B., "Two Color Particle Imaging Velocimetry," *J. of Laser Applications*, 1991, p.36.

Ruess, D.L., Adrian, R.J., Landreth, C.C., French, D.T., and Frasier, T.D., "Instantaneous Planar Measurements of Velocity and Large Scale Vorticity and Strain Rate in an Engine Using Particle Imaging Velocimetry," SAE Technical Paper 890616.

Goebel, S.G., and Dutton, J.C., "Velocity Measurements of Compressible Turbulent Mixing Layers," *AIAA J.*, In Press.

Chen, T. H. , Roe, L.A. , and Nejad, A.S., "Multifunction Doplet imaging and velocimetry system for spray jets." *J of Propulsion and Power*, Vol 10, 1996, p. 798.

Spina, E., Smits, A., and Robinson, S., "The Physics of Supersonic Turbulent Boundary Layers," *Annu. Rev. Fluid Mech.*, Vol 26, 1994, p. 287.

Miller, R., Dotter, J., Bowersox, R., and Buter, T., "Compressible Turbulence Measurements in Supersonic Boundary Layers with Favorable and Adverse Pressure Gradients," 2nd Symposium on Transitional and Turbulent Compressible Flows, *Joint ASME/JSME Fluids Engineering Conference*, FED - Vol. 224, 1995, p. 193.

Lempert W.R., Zhang, B., and Miles, R.B., "Stimulated Raman Scattering and Coherent Anti-Stokes Raman Spectroscopy in High Pressure Oxygen," *J. Opt. Soc. Am. B*, Vol. 7, No. 5, 1990, p. 715.

Bowersox R.D.W., and Buter T.A., "Mass-Weighted Turbulence Measurements in a Mach 2.9 Boundary Layer Including Mild Pressure Gradients," AIAA Paper #96-0659

Adrian, R.J., "Particle-Imaging Techniques for Experimental Fluid Mechanics," *J. of Fluid Mech.* Vol. 23, 1991, p. 261.

Tennekes, H. and Lumley, J.L., *A First Course in Turbulence*. Cambridge, MA: MIT Press, 1972, p. 248.

Molezzi, M.J., "Development and Application of Particle Image Velocimetry in High Speed Separated Flow: Two-Dimensional Base Cavities," Ph.D. Thesis, University of Illinois, Urbana-Champaign, 1993.

Adrian, R.J., Yao, C.-S., "Pulsed Laser Technique Application to Liquid and Gaseous Flows and the Scattering Power of Seed Materials," *Applied Optics*, Vol. 24, No. 1, 1985, p. 44.

Yao, C., and Paschal, K., "PIV Measurements of Airfoil Wake-Flow Turbulence Statistics and Turbulent Structures," AIAA Paper 94-0085, January 1994.

Bryanston-Cross, P.J., and Epstein, A., "The Application of Sub-Micron Particle Visualization for PIV (Particle Image Velocimetry) at Transonic and Supersonic Speeds," *Prog. Aerospace Sci.*, Vol. 27, No. 1990, pp. 237-265.

Goss, L.P., Post, M. E., Trump, D. D., and Sarka, B., "Two-Color Particle Imaging Velocimetry," *J. Laser Appl.*, Vol. 3, No. 1991, pp. 36-42.

Gogineni, S., and Trump, D., and Goss, L., "Two-Color PIV Employing a Color CCD Camera," *48th APS/DFD Meeting*, November 19-20, 1995. Abstract Pub. in *Bull. APS* 40(12), 1950(1995), 1995.

Adrian, R.J., "Particle Imaging Techniques for Experimental Fluid Mechanics," *Ann. Rev. Fluid Mech.*, Vol. 23, No. 1991, pp. 261-304.

Bowersox, R.D.W., and Buter, T. A., "Mass-Weighted Turbulence Measurements in a Mach 2.9 Boundary Layer Including Mild Pressure Gradients," AIAA Paper 96-0659, January 1996.

Dasgupta, S., Terry, W. F., Vuppuladhadiam, R., Bowersox, R. D. W., Glawe, D.D., Chen, T.H., and Nejad, A.S., "Two-Color Particle Imaging Velocimetry Systems for Supersonic Flow Studies," AIAA-96-2798, July 1996.

Gogineni, S., Trump, D., Goss, L., Rivir, R., Pestian, D., "High-Resolution Digital Two-Color PIV (D2CPIV) and Its Application to High Freestream Turbulent Flows," *Proceedings of the 8th International Symposium on Applications of Laser Techniques to Fluid Mechanics*, Lisbon, Portugal, 1996.

Kline, S.J., and McClintock, F. S., "Describing Uncertainties in Single Sample Experiments," *Mech. Eng.*, Vol. 75, No. 1953, pp. 3-8.

## **12. APPENDICES**

Please see attached documents.